Monthly Notices of the ROYAL ASTRONOMICAL SOCIETY

MNRAS **507,** 2300–2317 (2021) https://doi.org/10.1093/mnras/stab2257
Advance Access publication 2021 August 9

WALLABY pre-pilot survey: H I content of the Eridanus supergroup

B.-Q. For [1,2]★ J. Wang,[3] T. Westmeier [1,2] O. I. Wong [4,1,2] C. Murugeshan,[4,2] L. Staveley-Smith [1,2] H. M. Courtois,[5] D. Pomarède,[6] K. Spekkens,[7] B. Catinella [1,2] K. B. W. McQuinn,[8] A. Elagali,[9] B. S. Koribalski [10,11,2] K. Lee-Waddell [1,4] J. P. Madrid,[12] A. Popping,[1] T. N. Reynolds [1,2] J. Rhee,[1,2] K. Bekki,[1] H. Dènes,[13] P. Kamphuis[14] and L. Verdes-Montenegro[15]

[1]*International Centre for Radio Astronomy Research, University of Western Australia, 35 Stirling Hwy, Crawley, WA 6009, Australia*
[2]*ARC Centre of Excellence for All Sky Astrophysics in 3 Dimensions (ASTRO 3D)*
[3]*Kavli Institute for Astronomy and Astrophysics, Peking University, Beijing 100871, China*
[4]*CSIRO Space and Astronomy, PO Box 1130, Bentley, WA 6102, Australia*
[5]*Univ Claude Bernard Lyon 1, IP2I Lyon, IUF, F-69622 Villeurbanne, France*
[6]*Institut de Recherche sur les Lois Fondamentales de l'Univers, CEA Université Paris-Saclay, F-91191 Gif-sur-Yvette, France*
[7]*Royal Military College of Canada, PO Box 17000, Station Forces, Kingston, ON K7K 7B4, Canada*
[8]*Department of Physics and Astronomy, Rutgers University, 136 Frelinghuysen Road, Piscataway, NJ 08854, USA*
[9]*Telethon Kids Institute, Perth Children's Hospital, Perth, Nedlands, WA 6009, Australia*
[10]*CSIRO Space and Astronomy, PO Box 76, Epping, NSW 1710, Australia*
[11]*School of Science, Western Sydney University, Locked Bag 1797, Penrith, NSW 2751, Australia*
[12]*The University of Texas Rio Grande Valley, One West University Blvd, Brownsville, TX 78520, USA*
[13]*ASTRON, The Netherlands Institute for Radio Astronomy, Oude Hoogeveensedijk 4, NL-7991 PD Dwingeloo, the Netherlands*
[14]*Faculty of Physics and Astronomy, Astronomical Institute, Ruhr University Bochum, D-44780 Bochum, Germany*
[15]*Instituto de Astrofísica de Andalucía, CSIC, Glorieta de la Astronomía, E-18080 Granada, Spain*

Accepted 2021 July 30. Received 2021 July 29; in original form 2021 July 5

ABSTRACT

We present observations of the Eridanus supergroup obtained with the Australian Square Kilometre Array Pathfinder (ASKAP) as part of the pre-pilot survey for the Widefield ASKAP L-band Legacy All-sky Blind surveY (WALLABY). The total number of detected H I sources is 55, of which 12 are background galaxies not associated with the Eridanus supergroup. Two massive H I clouds are identified and large H I debris fields are seen in the NGC 1359 interacting galaxy pair, and the face-on spiral galaxy NGC 1385. We describe the data products from the source finding algorithm and present the basic parameters. The presence of distorted H I morphology in all detected galaxies suggests ongoing tidal interactions within the subgroups. The Eridanus group has a large fraction of H I-deficient galaxies as compared to previously studied galaxy groups. These H I-deficient galaxies are not found at the centre of the group. We find that galaxies in the Eridanus supergroup do not follow the general trend of the atomic gas fraction versus stellar mass scaling relation, which indicates that the scaling relation changes with environmental density. In general, the majority of these galaxies are actively forming stars.

Key words: galaxies: groups: general – galaxies: ISM – galaxies: star formation.

1 INTRODUCTION

The star formation–density and morphology–density relations highlight the dependence of galaxy evolution on environment. A galaxy cluster is the most striking place to look for environmental effects on galaxy evolution. Observations show that the star formation is suppressed in cluster environments (Gómez et al. 2003; Cortese et al. 2019) and the fraction of early-type (elliptical and lenticular) galaxies increase in denser cluster environments as compared to the fraction of late-type (spiral and irregular) galaxies (Dressler 1980; Postman et al. 2005). Recent studies of clusters in the local Universe have shown conflicting results. While a morphology–density relation remains within each halo, the total fraction of early-type galaxies is nearly constant across three orders of magnitude in cluster halo mass ($13 \leq \log M_{\rm h}/(h^{-1}\ {\rm M}_{\odot}) \leq 15.8$) (Hoyle et al. 2012). The study of Simard et al. (2009) also shows no clear trend of the early-type fractions in clusters as a function of cluster velocity dispersion. These results suggest that most morphological transformation is happening in groups prior to merging into massive clusters. The small velocity dispersion of galaxy groups also results in more galaxy mergers than in clusters (e.g. Hickson 1997). A combination of nature and nurture must be at play to drive such differences. The evolutionary effects imposed by different environments are important to understand.

In order to gain a full picture of galaxy evolution, it is crucial to investigate the gas and stellar content of galaxies. Hydrogen gas makes up the baryonic matter that is channelling through large-scale structure filaments to haloes, cooling to neutral form in galaxy discs, and then to molecular gas to form stars. Observations of H I are a direct way to trace recent and ongoing interaction between galaxies and their environment due to its large extent beyond the stellar disc (Hibbard & van Gorkom 1996). Interactions can occur via a number

★ E-mail: biqing.for@uwa.edu.au

of physical processes, such as cold gas accretion with fresh gas channelling from the intergalactic medium (IGM) directly into the galaxies, hot mode gas accretion with gas being shock heated to high halo virial temperatures and falling back to the galaxy centre as it cools (Katz et al. 2003; Kereš et al. 2005), tidal stripping due to gravitational interaction (Chung et al. 2009; For et al. 2014), and ram-pressure stripping when galaxies pass through a dense IGM (Kenney, van Gorkom & Vollmer 2004; Abramson et al. 2011). These processes largely contribute to gas removal and accretion in galaxies, which in turn, affect their star formation efficiency (Cortese, Catinella & Smith 2021).

There is evidence that galaxies have undergone 'pre-processing' in group environments before falling into clusters (Zabludoff & Mulchaey 1998; Mahajan 2013). Thus, galaxy groups are the ideal place for following the galaxy evolutionary path. In addition, galaxy groups are more common than clusters (Tully 2015, hereafter T15). Examples include the studies of the NGC 3783 group (Kilborn et al. 2006), the Sculptor group (Westmeier et al. 2017), NGC 2997 and NGC 6946 (Pisano 2014) using single-dish telescopes, and the Hickson compact groups using the interferometer (Verdes-Montenegro et al. 2001). Systematic surveys of a large sample of galaxy groups are not an easy task in part due to the trade-off between angular resolution and sensitivity. Single-dish telescopes provide excellent sensitivity but at arcminutes angular resolution. In order to resolve gas discs and H I debris, high angular resolution imaging with the use of interferometers is required. However, the required observing time is significantly more for an interferometer to reach the equivalent low H I column density sensitivity of a single-dish telescope. In addition, a traditional interferometer has a small field of view (FOV), which makes targeting clusters a better option for providing large samples than galaxy groups for the equivalent amount of observing time.

The Widefield ASKAP L-band Legacy All-sky Blind surveY (WALLABY; Koribalski et al. 2020) makes use of the large FOV capability of the Australian Square Kilometre Array Pathfinder (ASKAP; Johnston et al. 2007) to image H I galaxies out to a redshift $z \sim 0.26$ and across 3π sr of the sky ($-90^\circ < \delta < +30^\circ$). The estimated root-mean-square (rms) noise level is anticipated to be 1.6 mJy per beam per 18.5 kHz channel. The survey is expected to detect 500 000 galaxies (Koribalski et al. 2020). The main advantage of ASKAP over traditional radio interferometers is the use of a state-of-the-art phased array feed (PAF), which allows the formation of multiple beams on the sky simultaneously to achieve a fast survey speed. For WALLABY, the targeted angular and spectral resolution of 30 arcsec and 4 km s^{-1} at $z = 0$ are 2–30 times better than some of the single-dish surveys, most notably the H I Parkes All-Sky Survey (HIPASS; Barnes et al. 2001) and the Arecibo Legacy Fast ALFA (ALFALFA) survey (Giovanelli et al. 2005). WALLABY will revolutionize the H I extragalactic field by providing a large statistical sample of galaxies at high resolution across a wide range of environments from voids to groups and clusters.

To verify the observational feasibility of ASKAP and to improve the efficiency of the ASKAP data reduction pipeline, a WALLABY early science program was carried out in 2018 using 12–16 ASKAP antennas. Studies of the NGC 7162 group (Reynolds et al. 2019) and the Lyon Group of Galaxies 351 (LGG 351; For et al. 2019) show that the majority of galaxies in these groups are actively forming stars indicating inefficiency of gas removal processes in the loose group environment. H I debris due to tidal interaction has also been identified in the NGC 7232 galaxy group, with one gas cloud postulated to be the progenitor of a long-lived tidal dwarf galaxy (Lee-Waddell et al. 2019). Detailed studies of individual galaxies, NGC 1566 (Elagali et al. 2019) and IC 5201 (Kleiner et al. 2019), have also highlighted the importance of high-resolution imaging. The resolved H I kinematics allowed them to recover the dark matter fractions by modelling the observed rotational curves and to investigate the asymmetries of H I morphology of these galaxies.

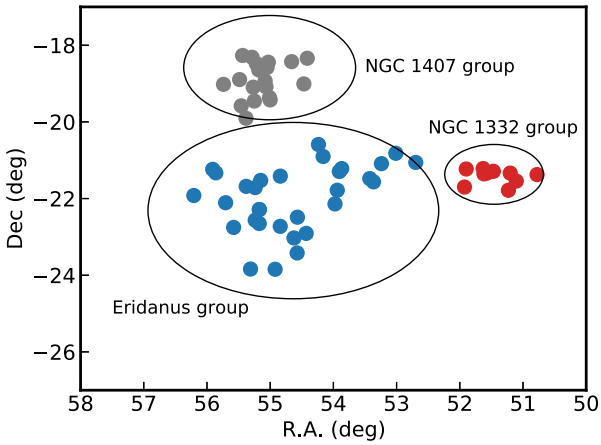

Figure 1. Distribution of galaxies in the Eridanus supergroup. Group members of NGC 1407, NGC 1332, and Eridanus groups as identified in B06 are represented by grey, red, and blue dots, respectively. The ellipses indicate that maximum radial extent of the groups.

1.1 Eridanus supergroup

Studies of the Eridanus concentration/region can be traced back to 1930s (see Baker 1933). A later in-depth study by de Vaucouleurs (1975) found that Group 31 along with galaxies associated with NGC 1332 and NGC 1209 formed the 'Eridanus Cloud'. This cloud lies on the Eridanus–Fornax–Dorado filamentary structure and is connected to the 'Great Wall' feature at ∼4000 km s^{-1} in the background (da Costa et al. 1988; Willmer et al. 1989). Several studies have shown the complex nature of the region. Willmer et al. (1989) showed that the region is made up of three or four subclumps, which are dynamically bound to each other and condensing to form a cluster. On the other hand, Omar & Dwarakanath (2005a) considered that the galaxies in the region as loose groups and in an intermediate evolutionary stage between the Ursa Major group and the Fornax Cluster. A reanalysis of this region using the 6dF Galaxy Survey (6dFGS; Jones et al. 2004) suggests that there are three distinct groups, namely the NGC 1407, NGC 1332, and Eridanus groups (Brough et al. 2006, hereafter B06). These groups also form part of the supergroup, which is defined as a group of groups that may eventually merge to form a cluster. Fig. 1 shows the group members as identified in B06.

The Eridanus supergroup is chosen as a pre-pilot field because it presents a different environment than the early science fields, which allows us to probe the subcluster merging/pre-processing scenario. It is thought to be an intermediate step of evolutionary path for clusters assembly, similar to the Ursa Major supergroup (Wolfinger et al. 2016). Our goals of this study are to investigate (1) the H I content of galaxies in the Eridanus field; (2) if the galaxies follow the typical H I scaling relation; (3) if their star formation rates reveal any difference in the merging/pre-processing environment; (4) if they are deficient in H I; and (5) if the H I deficiency parameter correlates with the projected distance from the group centre.

This paper is structured as follows. In Section 2, we describe the previous H I observations, ASKAP observations, its data reduction, and quality assessment. In Section 3, we describe the source finding

Table 1. ASKAP observations log of the Eridanus field.

UT date (yyyy-mm-dd)	Footprint	RA ($^{h}:^{m}:^{s}$)	Dec. ($^{\circ}\ ' \ ''$)	Calibrator SBID	Science SBID	Integration time (h)	Bandwidth (MHz)	Central frequency (MHz)
2019-03-13	A	3:39:30	−22:30:00	8169	8168	5.8	288	1295.5
2019-03-13	B	3:36:44.52	−22:37:54.69	8169	8170	5.0	288	1295.5

methodology, present the H I spectra, moment maps, mask, and signal-to-noise ratio (S/N) maps and compare the WALLABY integrated fluxes with previous H I studies. In Section 4, we redefine the Eridanus supergroup membership. In Section 5, we derive physical parameters: recession velocity, distance, H I linewidth, stellar mass, H I mass, and H I deficiency parameter. In Sections 6 and 7, we compare the derived quantities with the H I scaling relation and star-forming main sequence (SFMS). In Sections 8 and 9, we show a three-dimensional model of the environment the Eridanus supergroup resides in and a summary and conclusions. We also describe the H I and optical morphologies in Appendix A.

Throughout the paper, we adopt a Λ cold dark matter (ΛCDM) cosmology model with $\Omega_M = 0.27$, $\Omega_K = 0$, $\Omega_\Lambda = 0.73$, and $H_0 = 73\ \mathrm{km\ s^{-1}\ Mpc^{-1}}$. These are the default parameters for distances and cosmological-corrected quantities in the NASA/IPAC Extragalactic Database (NED) interface (Spergel et al. 2007).

2 DATA

2.1 Previous H I observations

The Eridanus field has previously been observed as part of the single-dish Parkes H I blind basketweave (BW) survey, with a follow-up study using the Australia Telescope Compact Array (ATCA; Waugh 2005) and one using the Giant Metrewave Radio Telescope (GMRT; Omar & Dwarakanath 2005a,b). The BW survey of the Eridanus field covered ∼100 deg^2 and is centred on $\alpha = 3^h22^m00^s$ (J2000), $\delta = -22^\circ00'00''$. The BW scanning technique was aimed at achieving higher sensitivity than HIPASS, with rms noise level a factor of 2 better (i.e. ∼7 mJy). The Hanning-smoothed velocity resolution is 26.4 km s^{-1}. The follow-up ATCA observations targeted 24 H I sources with a median rms of 6.5 mJy and a synthesized beam of ∼113 × 296 arcsec^2. Some of the H I sources remained unresolved. The GMRT also targeted the Eridanus supergroup with 46 scientifically usable observations out of the 57 observed targets. The primary beam of the GMRT observation is ∼24 arcmin. The GMRT final image cubes are either low resolution (∼50 arcsec) or high resolution (25 or 30 arcsec) with a velocity resolution of ∼13.4 km s^{-1}. The 3σ H I column density detection limit is $\sim 1 \times 10^{20}$ cm^{-2} for the GMRT high-resolution images.

2.2 ASKAP observations

Australian Square Kilometre Array Pathfinder (ASKAP) is a radio interferometer located in the remote outback of Western Australia and is part of the Murchison Radio-astronomy Observatory (MRO). It consists of 36 × 12 m^2 antennas, with each antenna equipped with a second-generation (Mk II) PAF. ASKAP is designed to provide an instantaneous large field of view (5.°5 × 5.°5) with 36 dual-polarization beams, a bandwidth of 288 MHz and high angular and spectral resolutions (McConnell et al. 2016; Hotan et al. 2021). During the interim period between the ASKAP early science program and the pilot survey, WALLABY carried out a pre-pilot survey targeting the Eridanus field in 2019 March. The survey attempted

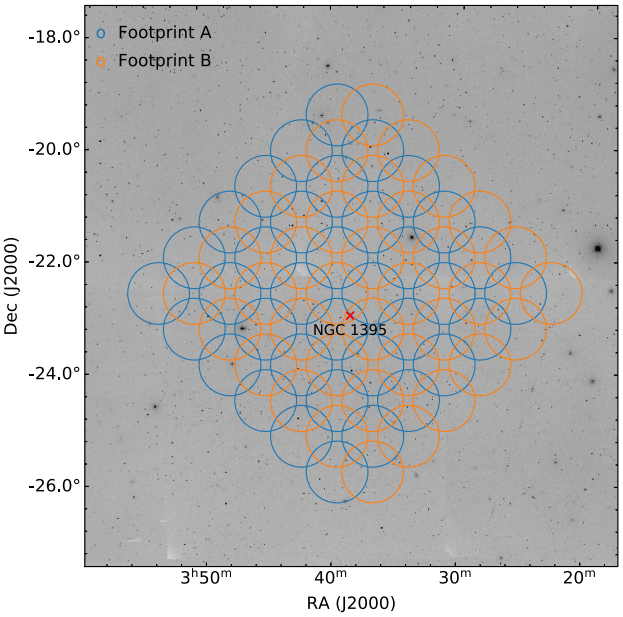

Figure 2. ASKAP footprints for the observations as listed in Table 1 overlaid on to the optical Digitized Sky Survey 2 (DSS-2) red image. The observed footprints have been rotated by position angle of 45° relative to a standard ASKAP footprint. Each beam has a full width at half-maximum (FWHM) of 1°. The blue and orange circles represent footprint A and B, respectively. The brightest elliptical galaxy, NGC 1395, in the Eridanus group is marked with cross.

to utilize the full 36 antennas for the two interleaving footprints (footprints A and B) in contrast to the 12–16 antennas and the multiple observations per footprint for the early science program.

Each footprint has a 6 × 6 beam pattern and was rotated by 45° on the sky. These observations were carried out during the day for footprint A and mostly at night time for footprint B. The primary calibrator, PKS 1934−638, was observed for about 2 h at the beginning of each observation. Each observation is given a scheduling block identification number (SBID),[1] and the total integration time for both footprints is 10.8 h. We present the observing log in Table 1 and the on-sky positions of interleaved footprints in Fig. 2.

2.3 Data reduction and quality assessment

The data are processed automatically using ASKAPSOFT version 0.24.7 (Whiting 2020; Wieringa, Raja & Ord 2020) installed on the 'Galaxy' supercomputer at the Pawsey Supercomputing Centre. Only baselines shorter than 2 km and half of the full 288 MHz bandwidth (i.e. 1295.5–1439.5 MHz) are processed. This is a huge improvement in data processing capability as compared to the early

[1]The SBID can be used to search for the corresponding data set in CSIRO ASKAP Science Data Archive (CASDA).

science program, in which only a small frequency range and few beams were processed at a given time (see e.g. For et al. 2019).

All 36 beams are used for bandpass calibration, and the autocorrelation of each beam measurement set is flagged out completely. Radio frequency interference (RFI) and antenna flagging are performed on a beam-by-beam basis. The overall flagged visibility fraction ranges from 10 to 30 per cent across all beams and the minimum number of utilized antennas per beam is 31. Subsequently, the derived bandpass solution is applied to each beam. Flux density calibration in each frequency channel is performed using PKS B1934−638 and gain calibration is performed via self-calibration. Continuum images of each beam are used as models to subtract continuum sources in the *uv* domain. For the final spectral line imaging, a pixel size of 6 arcsec is adopted. We use Wiener filtering with a robustness of 0.5 in addition to Gaussian tapering to a resolution of ∼30 arcsec. Multiscale CLEAN is used to deconvolve the image (Cornwell 2008). Once the spectral line image cube per beam is created, image-based continuum subtraction of the residual continuum emission is performed by fitting a low-order polynomial to each spectrum. Finally, we create a primary beam corrected beam-by-beam mosaic image cube. Channels in beams that are severely affected by artefacts have been masked out in the image cube. A particular type of artefact in the form of large-scale stripes across the beam is found to have been caused by deconvolution failing during the imaging step. The origin of the divergence comes from overflagging of channels that contain Galactic emission.

We evaluate the data quality of each footprint image cube based on a set of metrics. These metrics are established based on the data in the WALLABY early science field of M83 (For et al. 2019), and include rms, minimum, and maximum flux densities, 1 percentile noise level, and median absolute deviation of median flux (MADMF). Two sets of these values are calculated and recorded during the pipeline processing. Each set consists of values for three types of image cubes, i.e. before and after continuum subtraction image cubes and a residual image cube. The first and second sets give values for each channel of the mosaicked image cubes and for each channel of each beam, respectively. The rms values of the footprint A and B mosaics increase as a function of frequency (5–6 mJy), which is consistent with the theoretical rms trend. The rms values of combined mosaic across all beams vary from 2.4 to 4.4 mJy with central beams having the lowest rms noise level.

To evaluate the effect of broad-band RFI/artefacts, we examine the median absolute deviation of maximum flux density (MADMFD) of each beam. This metric is sensitive to strong artefacts. In Fig. 3, we show the variation of MADMFD, and the largest values correspond to the beams with artefacts. We also examine the distribution of flux density values for all voxels in each beam at the 1 percentile level. Excessive negative flux density is shown to be related to bandpass calibration and/or side lobe issues. We fit each distribution with a Gaussian and use the variance as a metric to determine if beams have been affected by those issues. The metric shows a similar result to that of MADMFD for this data set.

A stand-alone PYTHON script[2] is used to generate an HTMLstyle summary report for each SBID. This report provides basic observation information, statistical plots generated from the pipeline, plots for visibilities, antenna flagging statistics, etc. The report of each footprint is included along with the data release on CASDA.

[2]Available at https://github.com/askap-qc/validation/blob/master/wallaby_hi_val.py

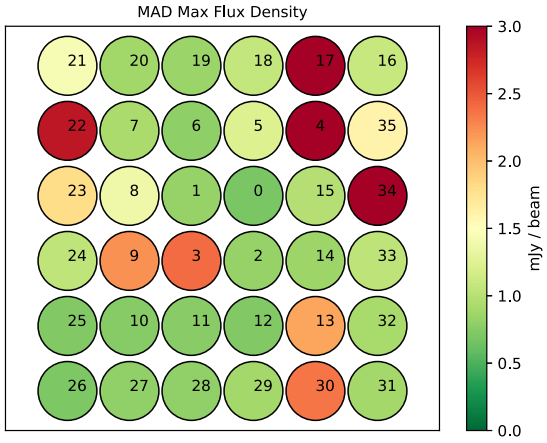

Figure 3. Median absolute deviation of maximum flux density (MADMFD) for each beam over frequency range 1295.5–1439.48 MHz for footprint A. Beam numbers for the ASKAP 6° × 6° footprint are labelled.

3 SOURCE FINDING AND CATALOGUING

We use the Source Finding Application (SOFIA;[3] Serra et al. 2015) version 2.0 (Westmeier et al. 2021) to search for H I sources in the mosaicked cube from $cz = 500$ to 8500 km s^{-1}. Channels that contain the Milky Way emission were excluded. SOFIA was set to automatically flag some known artefacts, such as continuum residuals or RFI, prior to the search. We scale the data by the local rms noise level and apply a threshold of 3.5σ for the smooth+clip source detection algorithm. A radius of 2 pixels and two spectral channels are used to merge the detected voxels into objects. SOFIA generates a cubelet, an associated mask cube, a signal map with the total number of H I detected channels for each pixel, a spectrum, integrated H I intensity (zeroth moment), velocity field (first moment), and velocity dispersion (second moment) maps for each detected source. To filter out false positive sources, SOFIA has implemented a reliability filter. The filter works by comparing the density of detections with positive and negative flux in parameter space to estimate the reliability of all positive detections under the principal assumption that astronomical sources must have positive flux, while the stochastic noise and any artefacts present in the data are symmetric about zero. A user-defined reliability threshold can then be applied to discard unreliable detections. We refer the reader to Serra, Jurek & Flöer (2012) for a detailed description of the reliability filter.

The final catalogue consists of 55 H I sources including two new H I sources (WALLABY J033911−222322 and WALLABY J033723−235753; see Wong et al. 2021) that do not have optical counterparts in Data Release 8 (DR8) Dark Energy Spectroscopic Instrument (DESI) Legacy Imaging Survey. The membership of each source is discussed in Section 4. In Fig. 4, we present the integrated H I intensity map of individual detected sources enlarged by a factor of 4.5 in the Eridanus supergroup and the full mosaic with all sources labelled by their designated catalogue identification number (ID) (refer to Table 3). Within the WALLABY Eridanus FOV, 38 galaxies were also observed by the GMRT. Among those, 22 are detected by both WALLABY and GMRT. The remaining 16 non-detections are detected by GMRT but not by ASKAP. As a blind survey, WALLABY recovers an additional 19 H I sources that were not targeted in the GMRT study.

[3]Available at https://github.com/SoFiA-Admin/SoFiA

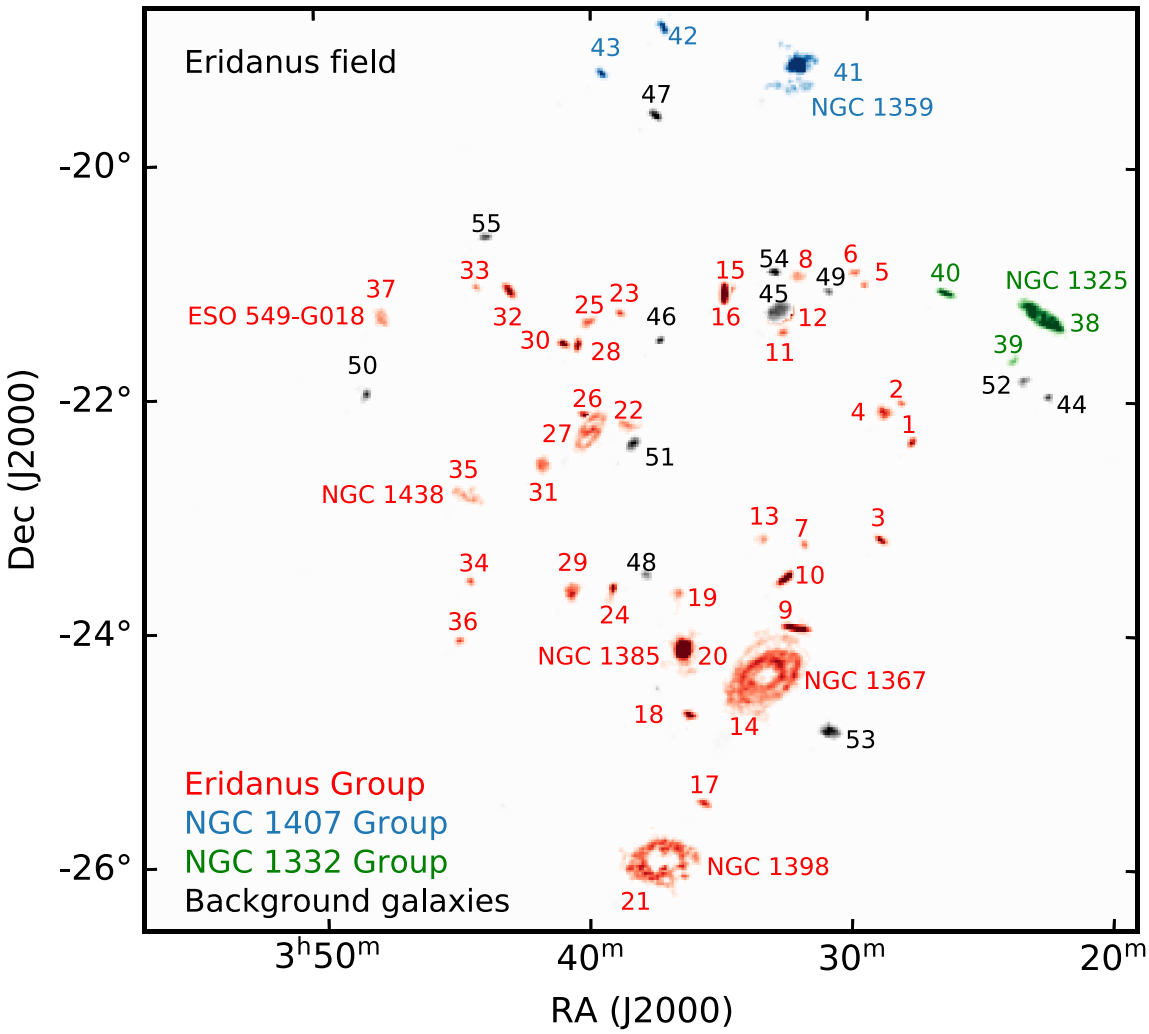

Figure 4. Integrated H I intensity map of individual sources in the Eridanus supergroup and in the background. Sources of the Eridanus group, the NGC 1407 group, the NGC 1332 group, and background galaxies are in red, blue, green, and black, respectively. All sources are enlarged by a factor of 4.5 for clarity. Designated ID number for all 55 H I detected sources is labelled.

3.1 H I intensity, velocity field, S/N maps, and H I spectra

We convert the H I intensity maps (Jy Hz) from SOFIA to integrated H I column density ($N_{\rm H\,I}$) maps by using equation (76) in Meyer et al. (2017). We also create 1σ flux density sensitivity maps by using the channel cubes from SOFIA. Subsequently, we divide each integrated H I column density map by its corresponding 1σ $N_{\rm H\,I}$ sensitivity map to obtain a signal-to-noise ratio (S/N) map. The S/N maps are used to clip the velocity field maps, in which pixels below a certain σ are masked out. The spectrum of each source is created by integrating the flux densities of all spatial pixels in each spectral channel (provided by SOFIA). Fig. 5 shows the $N_{\rm H\,I}$ contours overlaid on to the DR8 DESI Legacy Imaging Survey g-band co-added image[4] (refer to Section 5.3 for detail), clipped velocity field maps, and spectra in $V = cz$, where c is the speed of light and z is the H I derived redshift. Most of the detected galaxies are marginally resolved. Using these maps and images, we describe the H I and optical morphologies of individual galaxies in Appendix A.

[4]Co-added cutout images are available at https://datalab.noao.edu/ls/dataAccess.php

3.2 H I integrated flux

To obtain the integrated flux ($S_{\rm int}$) in Jy Hz, we sum the flux densities across all channels within the mask. To verify the measured $S_{\rm int}$ from WALLABY and for direct comparison with previous studies, we convert the values from Jy Hz to Jy km s^{-1}. In Fig. 6, we show the $S_{\rm int}$ comparison between BW and HIPASS (Meyer et al. 2004) catalogues (top panel), the $S_{\rm int}$ comparison between WALLABY and ATCA (middle panel), and the $S_{\rm int}$ comparison between WALLABY and the single-dish studies (bottom panel). The solid line represents the unity line. Overall, the $S_{\rm int}$ from two Parkes surveys are consistent with each other. For the interferometers comparison, there are outliers at the fainter end (<10 Jy km s^{-1}). The $S_{\rm int}$ values of fainter sources from ATCA are about a factor of 2 smaller than WALLABY's. We find that the $S_{\rm int}$ values of these outliers are also a factor of 2 lower than BW, which suggests that the issue is not related to WALLABY. However, there does appear to be some missing flux in the ASKAP/ATCA interferometer results relative to both Parkes studies.

For the outlier, NGC 1415, a clear systematic offset is seen between the WALLABY and single-dish data. For NGC 1415, we verify that HIPASS has only detected half of the galaxy. The missing fluxes

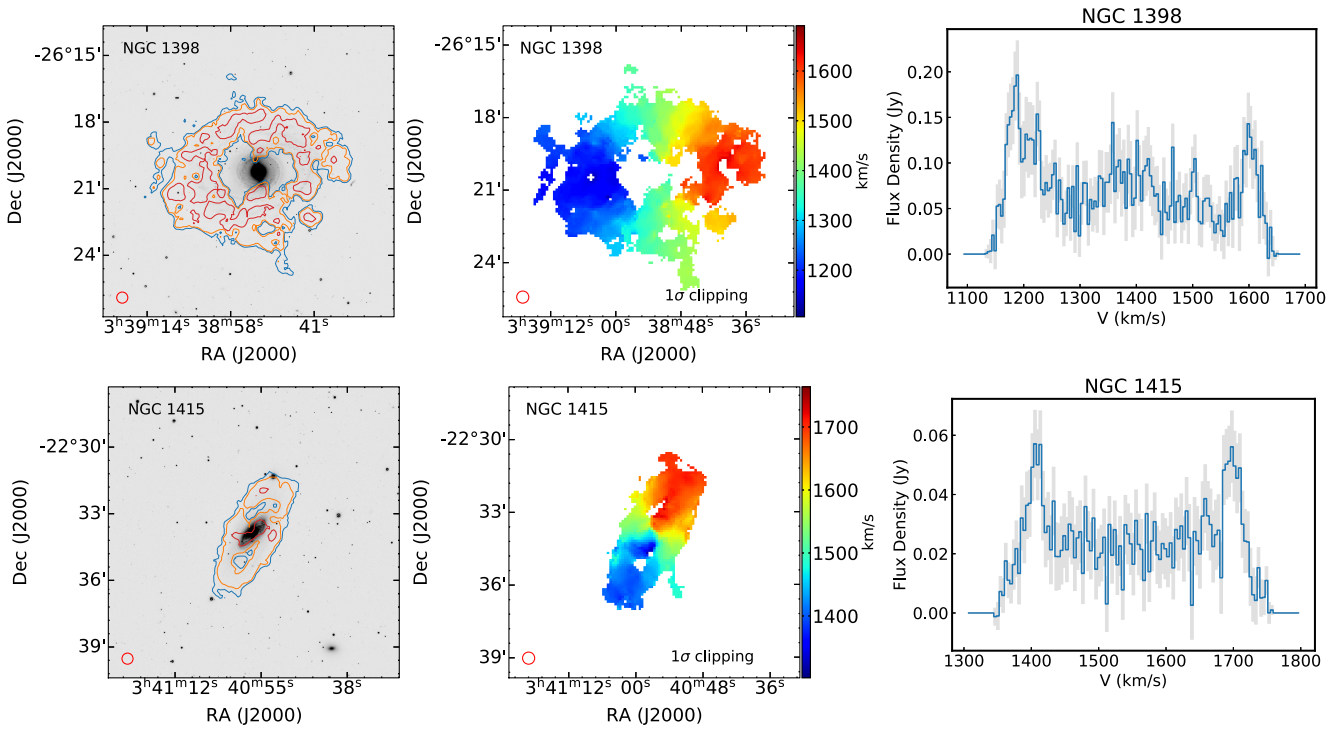

Figure 5. Examples of WALLABY H I sources. A mean correction factor of 20 per cent has been applied to integrated H I column density maps, flux density, and local rms of spectra. The synthesized beam of 30 × 30 arcsec^2 is plotted at the left-bottom corner of each subplot as a reference. Left: integrated H I column density maps of individual sources overlaid on to the DR8 DESI Legacy Imaging Survey *g*-band stacked images. The colour scale of blue, orange, red, purple, and olive green represent the contour levels of 1, 2, 5, 10, 20 × 10^{20} cm^{-2}, respectively. The 3σ of H I column density sensitivity level for a typical rms of 1.7 mJy beam^{-1} over 20 km s^{-1} is 1.2 × 10^{20} cm^{-2}. Middle: first moment velocity field maps of individual sources. Pixels above $n - \sigma$ are plotted and the value for n is given at bottom of each subplot. Right: spectra of individual sources derived by SOFIA. Grey area represents the upper and lower limit of uncertainties, $\sigma_{\rm rms}\sqrt{N_{\rm pix}/A_{\rm beam}}$, where the Gaussian beam area, $A_{\rm beam} = \pi\theta_{\rm bmaj}\theta_{\rm bmin}/(4\ln 2)$. Note: this figure is published in its entirety as Supporting Information with the electronic version of the paper. A portion is shown here.

for some of the bright WALLABY sources can be explained. For example, NGC 1359 is an interaction galaxy pair, which WALLABY has resolved into tidal debris (see Fig. 5). The diffuse emission is likely resolved out in this case. Both NGC 1398 and NGC 1359 are located in edge beams, where the noise level is significantly higher than in central beams. NGC 1367/NGC 1371 is a large galaxy with an H I diameter ($d_{\rm H I}$) as observed by the Green Bank Telescope (GBT) of 22.3 arcmin (Sorgho et al. 2019). Our zeroth moment map shows a $d_{\rm H I}$ of 9.9 arcmin, which indicates that our observation does not recover the extended H I disc of this galaxy. We cannot make a comparison with the GMRT study because they also lost flux for large galaxies due to inadequate sampling of short spacing data.

We further investigate the missing flux issue by comparing the non-confused continuum sources with the NRAO VLA Sky Survey (NVSS; Condon et al. 1998). We find that our sources are systematically 6 per cent lower in flux density than NVSS. However, the above issues (flux density calibration, sensitivity, and zero spacing) cannot fully account for the offset between WALLABY and single-dish data. Results from the Rapid ASKAP Continuum Survey (RACS; McConnell et al. 2020) have shown position-dependent variations of flux density due to inappropriate primary beam corrections. To circumvent this issue, holography beam measurements will be used as part of the instrumental flux calibration for future observations.

To estimate the systematic offset in H I fluxes, we compare the WALLABY data with all the single-dish data and fit an orthogonal distance regression (ODR) model. Both WALLABY and single-dish data errors are weighted for the ODR model (dashed line). We find a ∼20 per cent mean difference. For statistical purposes, we use this mean correction factor for the derived parameters for all sources for the rest of the paper. We also list the uncorrected $S_{\rm int}$.

4 GROUP MEMBERSHIP

By examining the older (Garcia 1993; Garcia et al. 1993, hereafter G93 for both) and newer (T15; Tully, Courtois & Sorce 2016, hereafter TCS16) galaxy group catalogues, we find that several galaxies are not included as part of the groups in B06. This is in part due to different methods and constraints being adopted for sample selection. G93 used a combination of friends-of-friends and Materne–Tully (Materne 1978; Tully 1980) methods to identify galaxy groups based on a galaxy sample with a *B*-band magnitude cut-off of 14.0 in the Lyon-Meudon Extragalactic Database (LEDA; Paturel et al. 1988). T15 defined the galaxy group differently based on Two Micron All Sky Survey (2MASS) data and used scaling relations as additional selection parameters. There are caveats for all of these methods and selection criteria.

In Fig. 7, we show the galaxy members of the NGC 1407 (grey), Eridanus (blue), and NGC 1332 (red) groups as identified in B06. The ellipses represent the maximum radial extent of the groups based on r_{500} (radius that encompasses overdensity of 500 times the critical density) in table 3 of B06. The encompassed virial masses are 7.9, 2.1, and 1.4 × 10^{13} M$_\odot$ for NGC 1407, Eridanus, and NGC 1332 groups, respectively. The locations of two detected

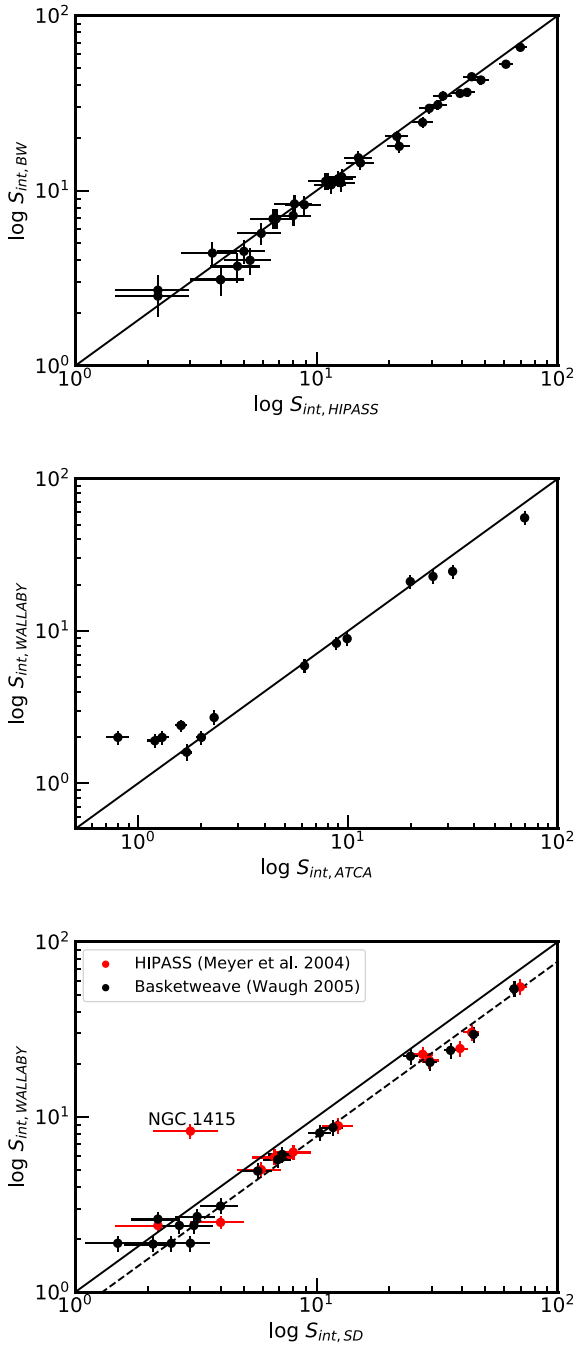

Figure 6. Comparison of $S_{\rm int}$ between various studies. The solid line is the 1:1 unity line. We adopt 10 per cent of $S_{\rm int}$ as errors for WALLABY data points as the statistical uncertainties as listed in Table 3 do not take into account calibration uncertainties. Top: comparison of $S_{\rm int}$ between BW (Waugh 2005) and HIPASS (Meyer et al. 2004). Middle: comparison of $S_{\rm int}$ between WALLABY pre-pilot and ATCA (Waugh 2005). Bottom: comparison of $S_{\rm int}$ between WALLABY pre-pilot and single-dish data. The black and red dots represent the $S_{\rm int}$ from BW and HIPASS, respectively. The dashed line is the fitted line, indicating a ∼20 per cent systematic offset between the WALLABY and single-dish data.

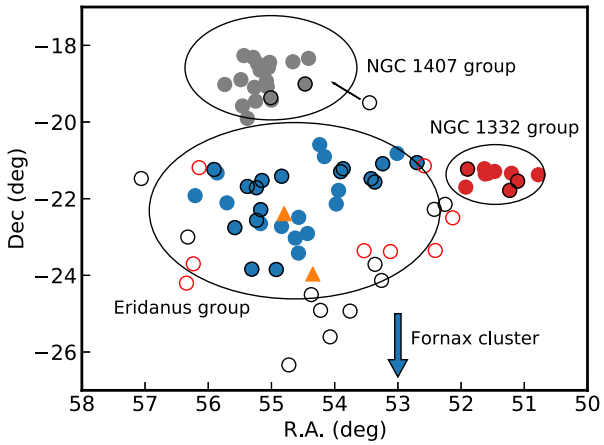

Figure 7. Same as Fig. 1 except adding detected H I sources in this study. Both red and black edge colour circles (including those filled) represent the detected H I galaxies. Two H I clouds are shown in orange triangles.

H I clouds are shown as orange triangles. The black and red edge colour circles represent the H I detected galaxies from this study. The former have been identified as group members in B06, G93, and/or T15 catalogues and the latter do not have a membership confirmation. These eight (open red circles) galaxies are relatively faint ($r > 15$ mag, see Table 4) and do not have 2MASS photometry. Thus, it is likely that these eight galaxies were missed in the T15 catalogue. To assess if these eight galaxies are associated with the Eridanus group, we calculate the velocity difference between each galaxy and the mean central velocity of the Eridanus group (1492 km s^{-1}) and then compare it to three times the velocity dispersion of 228 km s^{-1} (refer to T15 and TCS16). With this criterion, these eight galaxies are considered as part of the Eridanus group. We also consider detected H I galaxies in either B06, G93, and/or T15 as part of their associated groups. Table 2 summarizes the group membership identified in different catalogues and this study.

5 PHYSICAL PARAMETERS

The parameters derived in this section are given in Tables 3 and 4.

5.1 Distance and recession velocity

The recession velocity in the cosmic microwave background (CMB) reference frame, $V_{\rm CMB}$, is given by

$$V_{\rm CMB} = V_{\rm opt} + V_{\rm apex}[\sin b \sin b_{\rm apex} + \cos b \cos b_{\rm apex} \cos(l - l_{\rm apex})], \quad (1)$$

where l and b are Galactic coordinates, $l_{\rm apex} = 264.^{\circ}14$, $b_{\rm apex} = 48.^{\circ}26$, and $V_{\rm apex} = 371.0$ km s^{-1} (Fixsen et al. 1996). In Fig. 8, we show the $V_{\rm CMB}$ distribution of H I detected galaxies in the Eridanus field. The mean $V_{\rm CMB}$ for the Eridanus supergroup is ∼1500 km s^{-1}. The 'wall' behind the Eridanus supergroup at 4000 km s^{-1} is also shown. There are fewer galaxies beyond 4000 km s^{-1} as a result of decreasing sensitivity of the WALLABY data toward higher redshift.

For galaxies behind the Eridanus supergroup, we use $D_{\rm H} = V_{\rm CMB}/H_0$ and $D_{\rm L} = (1+z)D_{\rm c}$ to calculate the Hubble and luminosity distances, respectively. At low redshift ($z < 0.05$), the comoving distance, $D_{\rm c} \approx D_{\rm H}$, hence $D_{\rm L} \approx (1+z)D_{\rm H}$.

For the Eridanus subgroups, we consider redshift-independent measurements for their distances to avoid the effects of peculiar

Table 2. Group membership.

Designation	V (km s^{-1})	B06	G93	T15/TCS16	This study
(1)	(2)	(3)	(4)	(5)	(6)
			Group identification		
WALLABY J034002−192200	1216	NGC 1407	...	...	NGC 1407
WALLABY J033752−190024	1218	NGC 1407	...	...	NGC 1407
WALLABY J033019−210832	1226	...	...	...	Eridanus
WALLABY J033408−232125	1262	...	...	...	Eridanus
WALLABY J033047−210333	1292	Eridanus	...	...	Eridanus
WALLABY J033854−262013	1373	X 6dF	...	TSK 849, Nest 200100	Eridanus
WALLABY J032455−214701	1456	NGC 1332	...	...	NGC 1332
WALLABY J033501−245556	1458	X 6dF	...	TSK 849, Nest 200100	Eridanus
WALLABY J033723−235753[a]	1469	...	...	...	Eridanus
WALLABY J033728−243010	1497	X	LGG 97	TSK 849, Nest 200100	Eridanus
WALLABY J033327−213352	1509	Eridanus	...	...	Eridanus
WALLABY J033527−211302	1518	Eridanus	...	...	Eridanus
WALLABY J034517−230001	1546	X	LGG 97	TSK 849, Nest 200100	Eridanus
WALLABY J034056−223350	1552	Eridanus	...	TSK 849, Nest 200100	Eridanus
WALLABY J034219−224520	1569	Eridanus	...	...	Eridanus
WALLABY J034434−211123	1578	...	...	...	Eridanus
WALLABY J034814−212824	1586	X 6dF	LGG 97	TSK 849	Eridanus
WALLABY J032425−213233	1588	NGC 1332	...	TSK 849	NGC 1322
WALLABY J033617−253615	1590	X 6dF	...	Nest 200100	Eridanus
WALLABY J034337−211418	1612	Eridanus	...	...	Eridanus
WALLABY J033941−235054	1622	Eridanus	...	...	Eridanus
WALLABY J033921−212450	1622	Eridanus	...	...	Eridanus
WALLABY J032900−220851	1627	X	LGG 97	...	Eridanus
WALLABY J034131−214051	1644	Eridanus	...	...	Eridanus
WALLABY J034036−213129	1644	Eridanus	...	...	Eridanus
WALLABY J032937−232103	1657	X 6dF	...	...	Eridanus
WALLABY J033257−210513	1665	Eridanus	...	...	Eridanus
WALLABY J032735−211339	1686	NGC 1332	...	...	NGC 1332
WALLABY J034057−214245	1695	Eridanus	...	...	Eridanus
WALLABY J034522−241208	1733	...	...	...	Eridanus
WALLABY J032941−221642	1755	X 6dF	LGG 97	...	Eridanus
WALLABY J033228−232245	1755	X	...	...	Eridanus
WALLABY J034040−221711	1774	Eridanus	...	...	Eridanus
WALLABY J032831−222957	1774	...	...	...	Eridanus
WALLABY J033537−211742	1802	Eridanus	...	...	Eridanus
WALLABY J033326−234246	1810	X	LGG 97	Nest 200100	Eridanus
WALLABY J034456−234158	1819	X	...	...	Eridanus
WALLABY J033653−245445	1842	X	...	Nest 200100	Eridanus
WALLABY J033341−212844	1859	Eridanus	...	...	Eridanus
WALLABY J033911−222322[a]	1879	...	...	...	Eridanus
WALLABY J034114−235017	1885	Eridanus	...	Nest 200100	Eridanus
WALLABY J033302−240756	1915	X 6dF	...	Nest 200100	Eridanus
WALLABY J033347−192946	1964	X 6dF	LGG 100	TSK 863	NGC 1407

Note. Columns (1)–(2): designation and H I spectral line derived velocity – cz. Column (3): identification in B06 – member of Eridanus, NGC 1332, or NGC 1407 group; X represents galaxies that are not identified as any member of the groups but with 6dF identification; X 6dF indicates galaxies identified in NED but not observed in the 6dF survey. Column (4): identification in G93 – member of LGG 97 or LGG 100. Column (5): identification in T15 or TCS16 – member of TSK 849, TSK 863, and/or Nest 200100. Column (6): identification in this study. [a]H I clouds.

velocities, which are significant for galaxies with recession velocities less than 2000 km s^{-1} (Marinoni et al. 1998). There are several redshift-independent methods for determining distances, including the use of the globular cluster luminosity function (GCLF; Richtler 2003 and references therein). The GCLF is derived from the total observed population of globular clusters (GCs) of a galaxy. The distance modulus ($m - M$) derived from the GCLF of NGC 1407, NGC 1332, and NGC 1395 are 31.6 ± 0.1 mag (Forbes et al. 2006), 31.7 ± 0.24 mag (Kundu & Whitmore 2001), and 31.79 ± 0.16 mag (Escudero et al. 2018), respectively. These correspond to distances of 20.9, 21.9, and 22.8 Mpc. We note that the distance to the Eridanus group cannot solely rely on the measurement of NGC 1395 because it is not at the dynamical/virial centre of the group. Eridanus is dynamically young and is still evolving. Considering the distances and their associated errors of the more mature subgroups (NGC 1407 and NGC 1332), we adopt a distance of 21 Mpc for all subgroups.

5.2 H I linewidth

The H I linewidth measured at 20 per cent of the level of each peak (w_{20}) from SOFIA needs to be corrected for instrumental broadening.

Table 3. Source catalogue and derived parameters.

ID	Designation	Other ID	α (J2000)	δ (J2000)	$\nu_{\rm obs}$	z	V	$V_{\rm CMB}$	$D_{\rm H}$	$D_{\rm L}$	$S_{\rm int}$	$S^{\rm c}_{\rm int}$	$\mathrm{err}_{S^{\rm c}_{\rm int}}$	S/N	$w^{\rm c}_{20}$
			(°)	(°)	(MHz)		(km s^{-1})	(km s^{-1})	(Mpc)	(Mpc)	(Jy Hz)	(Jy Hz)	(Jy Hz)		(km s^{-1})
(1)	(2)	(3)	(4)	(5)	(6)	(7)	(8)	(9)	(10)	(11)	(12)	(13)	(14)	(15)	(16)
					Eridanus group										
1	WALLABY J032831−222957	ESO 481−G028	52.132460	−22.499216	1412.05	0.0059	1774	1643	21.0	21.0	5956	7147	629	11.4	91.4
2	WALLABY J032900−220851	ESO 548−G025	52.252679	−22.147546	1412.74	0.0054	1627	1495	21.0	21.0	3009	3611	467	7.7	135.5
3	WALLABY J032937−232103	ESO 481−G030	52.408316	−23.350973	1412.60	0.0055	1657	1528	21.0	21.0	9160	10 991	756	14.5	134.3
4	WALLABY J032941−221642	NGC 1347	52.424026	−22.278345	1412.14	0.0059	1755	1625	21.0	21.0	12 727	15 272	999	15.3	84.8
5	WALLABY J033019−210832	LEDA 832131	52.581366	−21.142435	1414.62	0.0041	1226	1095	21.0	21.0	2244	2692	458	5.9	49.7
6	WALLABY J033047−210333	ESO 548−G029	52.697580	−21.059272	1414.31	0.0043	1292	1161	21.0	21.0	4076	4892	619	7.9	138.5
7	WALLABY J033228−232245	ESO 482−G003	53.117925	−23.379351	1412.14	0.0059	1755	1630	21.0	21.0	3347	4017	465	8.6	69.6
8	WALLABY J033257−210513	ESO 548−G034	53.240898	−21.087152	1412.56	0.0056	1665	1537	21.0	21.0	5408	6490	740	8.8	84.5
9	WALLABY J033302−240756	ESO 482−G005	53.258442	−24.132440	1411.39	0.0064	1915	1793	21.0	21.0	29 797	35 756	1192	30.0	172.7
10	WALLABY J033326−234246	IC 1952	53.361541	−23.712911	1411.88	0.0060	1810	1688	21.0	21.0	23 915	28 698	1119	25.6	268.1

Note. This table is available in its entirety as Supporting Information with the electronic version of the paper. A portion is shown here for guidance regarding its form and content. Columns (1)–(3): identification number, designation, and other identification. Columns (4)–(5): α and δ (J2000) coordinates are based on H I detection. Column (6): $\nu_{\rm obs}$ is the detected central frequency of the H I detection. Column (7): z is redshift, defined as $z = (\nu_{\rm rest} - \nu_{\rm obs})/\nu_{\rm obs}$, where $\nu_{\rm rest}$ is H I rest frequency at 1420.405751 MHz and $\nu_{\rm obs}$ is the observed frequency. Column (8): $V = cz$. Columns (9)–(11): $V_{\rm CMB}$, $D_{\rm H}$, and $D_{\rm L}$ are recession velocity, Hubble distance, and luminosity distance (see Section 5.1). Columns (12)–(13): $S_{\rm int}$ and $S^{\rm c}_{\rm int}$ are integrated flux and corrected integrated flux (see Section 3.2). Column (14): $\mathrm{err}_{S^{\rm c}_{\rm int}}$ is statistical uncertainty of $S^{\rm c}_{\rm int}$, calculated as $\sigma_{\rm rms}\sqrt{N_{\rm pix}/A_{\rm beam}}\,\Delta\nu$, where the Gaussian beam area, $A_{\rm beam} = \pi\theta_{\rm bmaj}\theta_{\rm bmin}/(4\ln 2)$ and $\Delta\nu$ is the channel width in Hz. Column (15): S/N of $S^{\rm c}_{\rm int}$, calculated as $S^{\rm c}_{\rm int}/\mathrm{err}_{S^{\rm c}_{\rm int}}$. Column (16): $w^{\rm c}_{20}$ is H I linewidth measured at 20 per cent of the level of each peak corrected for instrumental broadening (see Section 5.2).

Table 4. Photometry, morphology, and derived parameters.

ID	Designation	Other ID	$E(B-V)$	g	r	M_r	$\log L_r$	$\log M_*$	$\log M_{\rm H\,I}$	$\mathrm{DEF}_{\rm H\,I}$	Morphology	Note
			(mag)	(mag)	(mag)	(mag)	($L_\odot$)	($M_\odot$)	($M_\odot$)			
(1)	(2)	(3)	(4)	(5)	(6)	(7)	(8)	(9)	(10)	(11)	(12)	(13)
						Eridanus group						
1	WALLABY J032831−222957	ESO 481−G028	0.0284 ± 0.0005	16.144	15.782	−15.829	8.176	8.05 ± 0.27	8.12 ± 0.22	0.06	...	Edge-on
2	WALLABY J032900−220851	ESO 548−G025	0.0324 ± 0.0012	14.652	14.066	−17.545	8.862	8.98 ± 0.25	7.82 ± 0.24	0.87	(R')SB(s)a	Peculiar
3	WALLABY J032937−232103	ESO 481−G030	0.0243 ± 0.0017	15.457	15.071	−16.540	8.460	8.36 ± 0.26	8.30 ± 0.21	0.09	Sc	...
4	WALLABY J032941−221642	NGC 1347	0.0355 ± 0.0011	13.594	13.194	−18.417	9.211	9.13 ± 0.23	8.45 ± 0.21	0.51	SB(s)c?	Peculiar, pair
5	WALLABY J033019−210832	LEDA 832131	0.0345 ± 0.0006	16.400	15.960	−15.652	8.105	8.07 ± 0.28	7.69 ± 0.26	0.43	...	Irr dwarf?
6	WALLABY J033047−210333	ESO 548−G029	0.0369 ± 0.0007	13.848	13.265	−18.346	9.182	9.30 ± 0.24	7.95 ± 0.24	0.98	SB?	...
7	WALLABY J033228−232245	ESO 482−G003	0.0299 ± 0.0009	15.845	15.541	−16.070	8.272	8.09 ± 0.27	7.87 ± 0.23	0.39	Sc	...
8	WALLABY J033257−210513	ESO 548−G034	0.0294 ± 0.0006	14.067	13.507	−18.104	9.086	9.18 ± 0.24	8.07 ± 0.23	0.79	SB?	LSB
9	WALLABY J033302−240756	ESO 482−G005	0.0261 ± 0.0008	14.994	14.620	−16.991	8.640	8.53 ± 0.25	8.81 ± 0.20	−0.29	SB(s)dm?	Edge-on
10	WALLABY J033326−234246	IC 1952[a]	0.0265 ± 0.0005	13.024	...	...	...	...±...	8.72 ± 0.20	...	SB(s)bc?	...

Note. This table is available in its entirety as Supporting Information with the electronic version of the paper. A portion is shown here for guidance regarding its form and content. Columns (1)–(3): identification number, designation, and other identification. Column (4): $E(B-V)$ is the Galactic dust extinction. Columns (5)–(6): intrinsic g- and r-band photometry derived from the DR8 Legacy Survey images (see Section 5.3). Columns (7)–(8): M_r and L_r are the r-band absolute magnitude and luminosity of the source (see Section 5.3). Column (9): $\log M_*/\mathrm{M}_\odot$ is the derived stellar mass in logarithm scale and error is derived from the error propagation equation with the assumption of 10 per cent uncertainty for the distance (see Section 5.3). Column (10): $\log M_{\rm H\,I}/\mathrm{M}_\odot$ is the derived H I mass using the corrected $S_{\rm int}$ in logarithm scale and error is derived from the error propagation equation with the assumption of 10 per cent uncertainty for the distance (see Section 5.4). Column (11): $\mathrm{DEF}_{\rm H\,I}$ is the H I deficiency parameter (see Section 5.4). Columns (12)–(13): morphology classification from NED and note for the source from this study. LSB: low surface brightness galaxy. [a]r-band image has been contaminated with artefact.

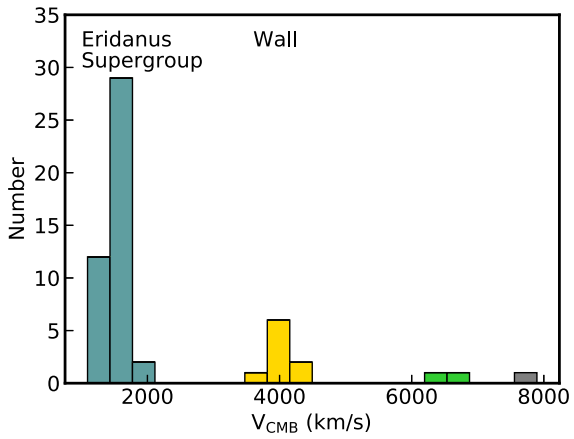

Figure 8. Histogram of recession velocities (V_{CMB}). Different colours represent H I detections in different groups of velocity.

The correction is given by

$$w_{20}^{c} = \frac{\sqrt{w_{20}^{2} - (\Delta s)^{2}}}{\Delta \nu} \Delta V_{\rm rest}. \quad (2)$$

w_{20} has a default unit of Hz from SOFIA. The instrumental broadening $\Delta s = 2\Delta\nu\lambda$, where λ is the broadening parameter and $\Delta\nu$ is assumed to be equal to the observed channel width in Hz (Springob et al. 2005). We adopt $\lambda = 0.5$ for a typical profile shape. The channel width in the source rest frame ($\Delta V_{\rm rest}$) in units of km s^{-1} can be calculated using the following equation:

$$\Delta V_{\rm rest} \simeq \Delta\nu \frac{c(1+z)}{\nu_{\rm H\,I}}, \quad (3)$$

where c is the speed of light, z is redshift, and $\nu_{\rm H\,I}$ is rest frequency of the H I emission line (Meyer et al. 2017). Subsequently, equation (2) can be simplified as follows:

$$w_{20}^{c} = \sqrt{w_{20}^{2} - (\Delta s)^{2}} \frac{c(1+z)}{\nu_{\rm H\,I}}. \quad (4)$$

5.3 Stellar mass

We use the existing colour–stellar mass relations of Bell et al. (2003, hereafter B03) to derive stellar masses of our galaxies. This relies on the photometry measurements from the co-added images of the DR8 DESI Legacy Imaging Surveys (Dey et al. 2019), which are primarily based on the Dark Energy Camera Legacy Survey (DECaLS) southern observations. The straightforward way to obtain co-added images is through the cutout tool, in which the acquired galaxy is centred and stitched if it falls between two or more CCD tiles. However, these cutout images are weighted averages of the individual images and subjected to varying point spread functions (PSFs). To verify if the use of such co-added cutout images would result in inaccurate photometry measurements, we obtain another set of co-added images by first finding out the identification names of the bricks in which galaxies are located and then retrieving the co-added images via the National Energy Research Scientific Computing Center (NERSC) server.[5] By comparing five fluxes obtained from cutout and non-cutout (non-stitched) co-added images, we find that the difference is small and within 0.02 mag. This implies that the issue with varying PSF is minor and we decide to use the cutout co-added images for the measurement to bypass the effort of stitching non-cutout co-added images manually.

We perform the g- and r-band photometry measurement using PROFOUND (Robotham et al. 2018). PROFOUND is used in rather than the traditional circular or ellipse-based method because it is useful for measuring fluxes of low surface brightness (LSB) galaxies, detecting faint signal with high noise level background and isolating foreground/background objects. Our sample consists faint dwarfs and LSB galaxies. To identify background objects, we use the three-colour composite images for guidance. The background galaxies tend to be redder in colour. We also cross-check the PROFOUND photometry measurements of a few bright galaxies with the DR8 tractor catalogue and find them to be consistent within 0.02 mag.

To calculate the extinction-corrected (intrinsic) magnitude, we adopt the wavelength-dependent extinction law that is parametrized by $R_V = A_V/E(B-V)$ (Cardelli, Clayton & Mathis 1989). Using the reddening law in Fitzpatrick (1999) and with $R_V = 3.1$, the tabulated A_λ values for Dark Energy Survey (DES) g and r bands are $A_g = 3.237\ E(B-V)$ and $A_r = 2.176\ E(B-V)$, respectively (see table 6 of Schlafly & Finkbeiner 2011). We estimate the Galactic dust extinction, $E(B-V)$, by using the recalibrated Schlegel–Finkbeiner–Davis (SFD) all-sky extinction maps (Schlegel, Finkbeiner & Davis 1998; Schlafly & Finkbeiner 2011). The intrinsic magnitude is then calculated as $\rm mag_0 = mag - A_\lambda$. Subsequently, we obtain the stellar masses by employing the mass-to-light ratio (M/L) relation in B03 as follow:

$$\log\left(\frac{M_*}{L_r}\right) = -0.306 + 1.097(g-r), \quad (5)$$

where L_r (luminosity) $= M_{r,\rm abs} - M_{\rm sun,abs}$ in $L_\odot$. The absolute magnitude of the Sun ($M_{\rm sun,\,abs}$) of different DES wavebands is given in Willmer (2018) and the D_L in Table 3 is used to calculate the $M_{r,\rm abs}$. This M/L relation adopts the 'diet' Salpeter (1955) initial mass function (IMF) that contains only 70 per cent of the mass due to a lower number of faint low-mass stars in their samples. To use the Chabrier (2003) IMF, the M_* values need to be scaled by 0.61 according to Madau & Dickinson (2014). This is to put our data points on the same scale with other surveys for comparison in Section 6.

We find that stellar masses for galaxies in the Eridanus supergroup and background galaxies range from 1.2×10^6 to 9.5×10^{10} $M_\odot$ and 6.3×10^7 to 2.1×10^{10} $M_\odot$, respectively. By comparing the scaled stellar masses with those calculated with the M/L–colour relations of Zibetti, Charlot & Rix (2009, hereafter Z09), we find that the difference is relatively small with an average ± 0.02 dex for all galaxies. The galaxies with high stellar mass ($M_* \gtrsim 10^{10}$ $M_\odot$) tend to have lower derived M_* when using the colour–stellar mass relations of B03. Using the colour–stellar mass relations of Z09, the lowest mass galaxy (WALLABY J033408−232125) in this study is 0.32 dex smaller in stellar mass. The differences are in part due to different stellar population synthesis models being adopted in the two studies (see Z09 for a detailed discussion). We adopt the stellar masses derived from B03. We do not find that the differences alter our conclusions.

5.4 H I mass and H I deficiency parameter

Assuming that the H I sources are optically thin, we can calculate the H I mass using the following equation:

$$\left(\frac{M_{\rm H\,I}}{M_\odot}\right) \simeq 49.7 \left(\frac{D_L}{\rm Mpc}\right)^2 \left(\frac{S_{\rm int}}{\rm Jy\ Hz}\right), \quad (6)$$

[5] Available at https://portal.nersc.gov/project/cosmo/data/legacysurvey/dr8/south/coadd/

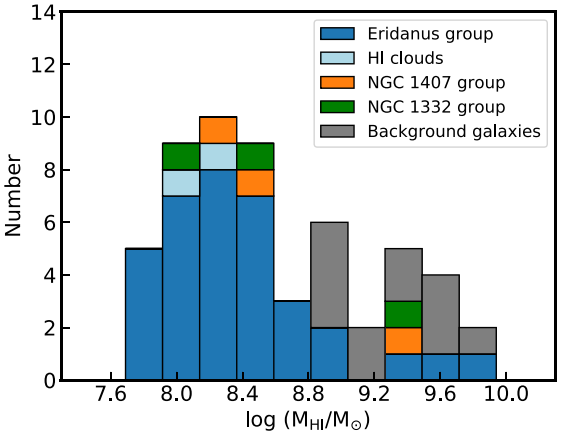

Figure 9. Histogram of H I masses on a logarithmic scale. Galaxies and H I clouds in the Eridanus group are represented in blue and light blue. Galaxies in the NGC 1407 group, the NGC 1332 group, and background are also represented in orange, green, and grey, respectively.

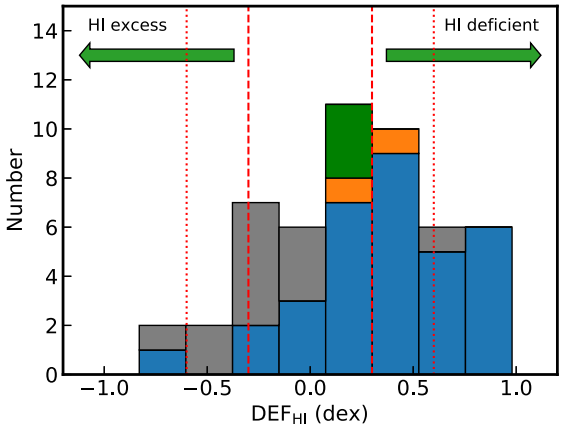

Figure 10. Same as Fig. 9 except on the distribution of H I deficiency parameter. The red dashed lines mark the boundaries of galaxies with normal H I content ($-0.3 < \mathrm{DEF_{H\,I}} < +0.3$) with respect to the expected H I from the scaling relation of D14. Galaxies with $\mathrm{DEF_{H\,I}} > +0.3$ and $\mathrm{DEF_{H\,I}} < -0.3$ are considered H I deficient and H I excess, respectively. The red dotted lines indicate the conservative definition of H I deficient and H I excess, i.e. $\mathrm{DEF_{H\,I}} > +0.6$, and $\mathrm{DEF_{H\,I}} < -0.6$.

where D_L is the luminosity distance and S_int is the integrated flux (Meyer et al. 2017). In Fig. 9, we show the histogram of the H I masses of the detected galaxies and H I clouds in the Eridanus group (blue and light blue), galaxies in the NGC 1407 and NGC 1332 groups (orange and green), and background galaxies (grey). The background galaxies have a H I mass distribution of $\sim 10^{8.9-10}$ $\mathrm{M_\odot}$. The H I mass of the Eridanus supergroup covers a range of $10^{7.7-9.8}$ $\mathrm{M_\odot}$ and has a median value of $10^{8.3}$ $\mathrm{M_\odot}$. We have recovered a significant number of galaxies with H I masses lower than those found in Omar & Dwarakanath (2005b), where their derived H I mass ranges from $\sim 10^{8.3}$ to $10^{9.9}$ $\mathrm{M_\odot}$.

To quantify the relative H I content of galaxies, we use the H I deficiency parameter, $\mathrm{DEF_{H\,I}}$. It is defined as the logarithmic difference between the expected and observed H I masses of a galaxy,

$$\mathrm{DEF_{H\,I}} = \log(M_{\mathrm{H\,I,exp}}/\mathrm{M_\odot}) - \log(M_{\mathrm{H\,I,obs}}/\mathrm{M_\odot}) \quad (7)$$

(Haynes & Giovanelli 1984). The expected H I mass of each galaxy can be determined by its morphology and size (Haynes & Giovanelli 1984; Solanes, Giovanelli & Haynes 1996; Jones et al. 2018) or magnitude-based H I scaling relations (Dénes, Kilborn & Koribalski 2014, hereafter D14). The morphology and size method is subject to inhomogeneous morphological classification and mostly limited to bright galaxies with known classification from previous studies. We have explored this method and find it unsuitable for our study given that there is a large number of new LSB galaxies and dwarfs without a homogenous morphological classification. Thus, we adopt the magnitude-based H I scaling relation to determine the expected H I mass, which is given by

$$\log(M_{\mathrm{H\,I,exp}}/\mathrm{M_\odot}) = 3.43 - 0.3 \times M_r, \quad (8)$$

where M_r is the absolute magnitude in the Sloan Digital Sky Survey (SDSS) r band[6] (see table 3 of D14). We consider a galaxy to be H I deficient if $\mathrm{DEF_{H\,I}} > +0.3$ and H I excess if $\mathrm{DEF_{H\,I}} < -0.3$. These criteria correspond to less than half or more than twice H I mass on average than expected. The histogram of $\mathrm{DEF_{H\,I}}$ for all galaxies is shown in Fig. 10. 20 galaxies are considered to be H I deficient and one H I excess in the Eridanus group. There is one H I-deficient galaxy within our limited sample of the NGC 1407 group. There are also four background galaxies considered to be H I excess, and with one galaxy considered to be H I deficient.

The on-sky distribution of $\mathrm{DEF_{H\,I}}$ of galaxies in the Eridanus supergroup is shown in Fig. 11, where the majority of H I-deficient galaxies are in close proximity with other H I detected galaxies. We note that the empirical scaling relation has a large intrinsic scatter with stellar luminosity alone as a prediction of H I mass. A more physically motivated derivation of the H I deficiency parameter has been explored using the stellar mass and angular momentum (see Obreschkow et al. 2016; Li et al. 2020). This method is adopted and the interpretation of H I deficiency of galaxies is further discussed in Murugeshan et al. (2021).

Overall, the Eridanus group consists of more H I-deficient galaxies than other Local Volume galaxy groups (see e.g. Reynolds et al. 2019). We also find that the H I deficiency parameter does not show any correlation as a function of projected distance from the Eridanus group centre. This is consistent with the study of H I galaxies in 16 loose groups, where H I-deficient galaxies are not necessarily found at the centres of groups but within ∼1 Mpc from the group centre (Kilborn et al. 2009). The non-correlation suggests that the pre-processing in the Eridanus group is yet to reach a stable stage of evolution. This is somewhat expected for a dynamically young system that is in the process of merging.

6 ATOMIC GAS FRACTION–STELLAR MASS SCALING RELATION

The atomic gas fraction ($M_{\mathrm{H\,I}}/M_*$) versus stellar mass scaling relation is a useful tool in investigating the influence of different environments on galaxy properties and H I content. In Fig. 12, we show the atomic gas fraction as a function of stellar mass. The top-left shows the extended *GALEX* Arecibo SDSS Survey (xGASS) H I detected sample (grey circles; Catinella et al. 2018), ALFALFA.40 samples (blue and red squares; Maddox et al. 2015), and samples from this study (orange and black circles). xGASS is a stellar mass selected H I survey and its sample is limited to $9 < \log\,(M_*/\mathrm{M_\odot}) < 11.5$ and $0.01 < z < 0.05$. The xGASS sample shows a clear trend of linear relation of decreasing $\log M_{\mathrm{H\,I}}/M_*$ with increasing

[6]SDSS r band is similar to the r band in DECaLS (Dey et al. 2019).

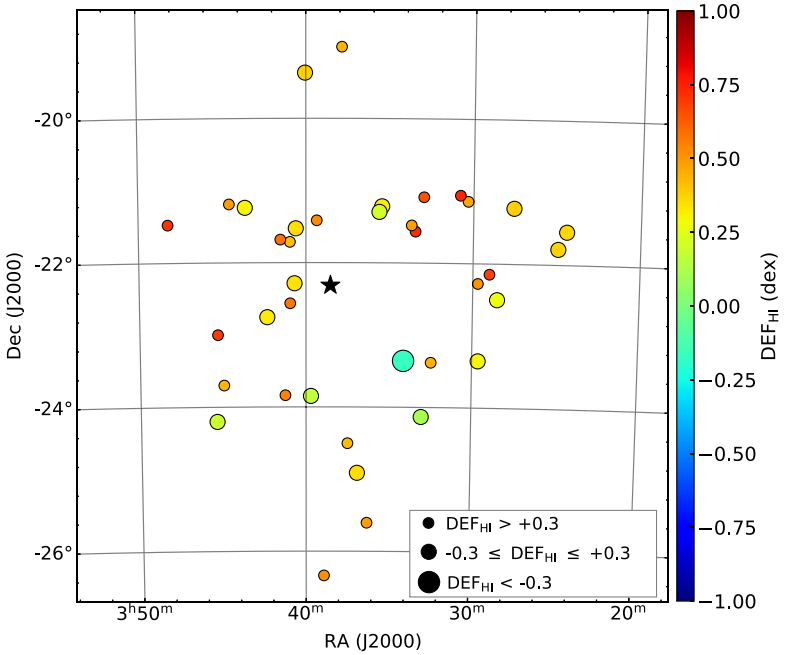

Figure 11. On-sky distribution of H I deficiency parameters of galaxies in the Eridanus supergroup. Colour and size correspond to their $\mathrm{DEF_{H\,I}}$. The Eridanus group centre is marked with the star.

$\log M_*$. The blue and red squares represent the atomic gas fraction (median $\log M_{\mathrm{H\,I}}$–$\log M_*$) of ALFALFA.40 samples with stellar masses derived from SDSS spectra and photometry, respectively (see tabulated values in table 1 of Maddox et al. 2015). These empirical relations show that the gas fraction follows the same trend as in the study of xGASS at higher stellar mass ($>10^9$ $\mathrm{M_\odot}$) but flatten out at lower stellar mass indicating relatively higher gas content in this regime. Deviation at the lower stellar mass end is seen between the two SDSS samples. The transition to this plateau presumably traces a real change in galaxy population as galaxies with high gas content ($M_{\mathrm{H\,I}}/M_* \sim 100$) would have been detected by ALFALFA.40.

Our data for the Eridanus supergroup and background galaxies are represented in orange and black circles, respectively. We find that galaxies in the Eridanus supergroup tend to have a lower atomic gas fraction for a given stellar mass than our background or xGASS or Maddox's galaxies. In top right-hand panel of Fig. 12, we show the trend being consistent with Local Volume H I Survey (LVHIS; Koribalski et al. 2018), Virgo Cluster only *Herschel* Reference Survey (HRS; Boselli et al. 2014), The H I Nearby Galaxy Survey (THINGS; Walter et al. 2008), and Faint Irregular Galaxies GMRT Survey (FIGGS; Begum et al. 2008) samples presented in Wang et al. (2017, hereafter W17).[7] The dashed line is a robust median linear fit of the data in W17, $\log(M_{\mathrm{H\,I}}/M_*) = -0.63 \times \log M_* + 5.07$, and it is used as a guide for the trend only. As stated in W17, such lower atomic gas fraction trend is a result of the selection effect and is not caused by the use of interferometer versus single-dish data. We also rule out the use of different colour–stellar mass relations and errors of stellar/H I masses as the cause of this trend for galaxies in the Eridanus supergroup. The shift in trend toward lower atomic gas fraction is not caused by the closer versus further distance of the sample either, as can be supported by the following test. If the bias is due to the H I detection limit, we expect the data points of Eridanus supergroup galaxies to be shifted upward once they are placed in the same distance as background galaxies. To achieve this, we assume a distance of 52 Mpc (comparable to the distance of our background galaxies) and calculate their S/N of S_{int}. We consider those with S/N of $S_{\mathrm{int}} \geq 5.9$ to be detectable at this assumed distance (see bottom left-hand panel). This value is the lowest detectable S/N of S_{int} of our galaxies sample (see Table 3). We find that the lower gas fraction trend remains when comparing to our background galaxies. This indicates that environmental effects might be at play for the galaxies in the Eridanus supergroup. It would be interesting to revisit the H I scaling relation with the full WALLABY survey using group, void, and cluster samples to probe the environmental effects in the future.

We also investigate the trend in the low-mass regime by overplotting the gas-rich Local Volume dwarf samples selected from ALFALFA.40 (Huang et al. 2012) (green circles), ultrafaint dwarf satellites of the Milky Way studied by Westmeier et al. (2015) (blue circles), sample from the Survey of H I in Extremely Low-mass Dwarfs (SHIELD; McQuinn et al. 2021, hereafter MQ21) (yellow triangles), 'almost dark' galaxies, Leo T and Leo P (Ryan-Weber et al. 2008; McQuinn et al. 2015; Adams & Oosterloo 2018) (green and red crosses) on to the scaling relation as shown in the bottom right-hand panel of Fig. 12. Sample of Huang et al. (2012) is a subset of ALFALFA.40, which stellar masses etc. of H I selected dwarf galaxies are rederived via the spectral energy distribution (SED) fitting. The selection eliminates the bias of ALFALFA.40 sample that tends to underestimate the stellar masses of low-mass galaxies with the SDSS reduction pipeline. This bias contributes to a higher gas fraction and the flattening trend at the low-mass end as seen in Maddox et al. (2015). The SHIELD dwarf galaxies sample ($M_{\mathrm{H\,I}} \lesssim 10^{7.2}$ $\mathrm{M_\odot}$) is a volumetrically complete H I selected sample from ALFALFA. The overall gas fraction as a sample group is slightly lower than Huang's but within the scatter. We note that the SHIELD sample mostly consists of isolated dwarf galaxies.

As for the ultrafaint dwarf samples, the gas fraction being presented here are their upper limit. It is known that dwarf satellites

[7]Chabrier IMF and $H_0 = 70$ km s^{-1} Mpc^{-1} were adopted.

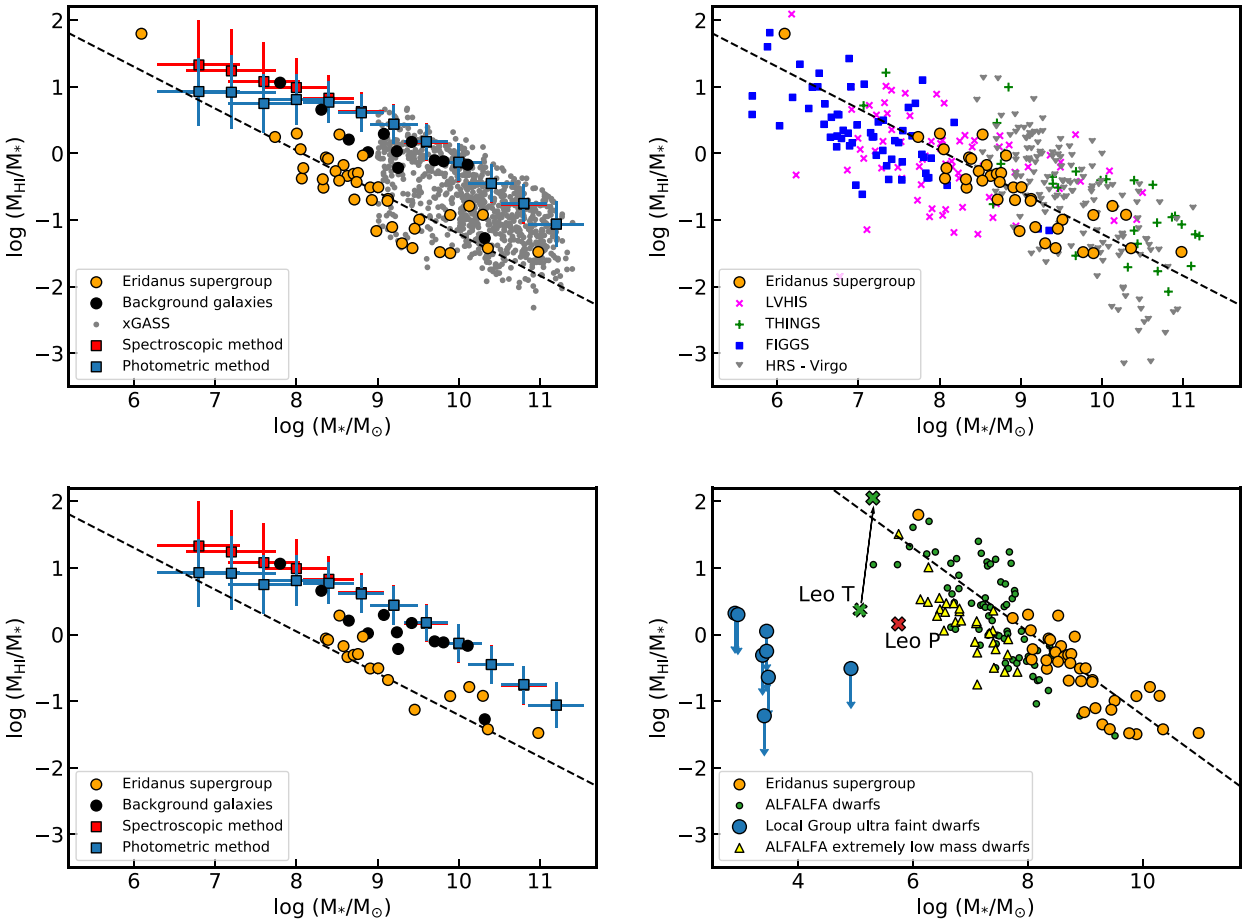

Figure 12. Atomic gas fraction scaling relation in logarithm scale ($\log(M_{\rm H\,I}/M_*)$ versus $\log M_*$). Top-left: Eridanus supergroup and background galaxies in this study are represented by orange and black dots, respectively. xGASS H I detected sample is in grey dots. The empirical relations derived from ALFALFA.40, SDSS spectroscopic (blue square) and photometric (red square) are overlaid on to the plot. Top-right: LVHIS (magenta crosses), THINGS (green pluses), HRS – Virgo Cluster members only (grey triangles), and FIGGS (blue squares) samples. The dashed line is used as a guide for the trend. Galaxies in the Eridanus supergroup (orange dots) are also overplotted and scaled to Chabrier IMF. Other studies used $H_0 = 70$ km s^{-1} Mpc^{-1}, which the resulting H I and stellar masses are still within errors of our derived $M_{\rm H\,I}/M_*$ and M_*. Bottom-left: same as top left-hand panel except with Eridanus supergroup galaxies that are detected at an assumed distance of 52 Mpc. Bottom-right: adding dwarf galaxies from ALFALFA.40 subsample (green dots), dwarf satellites within the Milky Way (blue circles), extremely low-mass dwarfs from ALFALFA (yellow triangles), Leo T (green cross), and Leo P (red cross) for comparison. The shift of the Leo T data point is due to the use of a different $M_{\rm H\,I}$.

located within the Local Group are H I deficient (Grcevich & Putman 2009; Putman et al. 2021). The loss of gas in these satellites is hypothesized to be the result of tidal interaction and ram-pressure stripping during perigalactic passages. The plot shows that the gas fraction of the dwarfs in the Local Group does not follow the general trend of the Local Volume ($M_* < 10^6$ M$_\odot$), although a future study is needed with a larger sample. It is also interesting to note that both Leo T (adopt $M_{\rm H\,I}$ of Leo T in Ryan-Weber et al. 2008) and Leo P appear to be outliers and are located closer to the ultrafaint dwarf samples on the guided H I scaling relation. If we adopt the $M_{\rm H\,I}$ of Leo T in the latest study of Adams & Oosterloo (2018), the data point falls on to the guided H I scaling relation. This is the result of a significant amount of faint H I emission being recovered with deep H I observations. It is unclear if this would be the case for Leo P.

7 STAR FORMATION RATE

To derive the star formation rate (SFR), we use the W4 band of the *NEOWISE* resolution enhanced mosaics (HiRes; Masci & Fowler 2009), far-ultraviolet (FUV) and near-ultraviolet (NUV) images of the *Galaxy Evolution Explorer* (*GALEX*; Martin et al. 2005).[8] We follow the method as described in W17 to perform the photometric measurements of these images for our galaxies. Subsequently, we calculate the total SFR as follows:

$$\mathrm{SFR}\ (\mathrm{M}_\odot\ \mathrm{yr}^{-1}) = \mathrm{SFR}_{\mathrm{FUV/NUV}} + \mathrm{SFR}_{\mathrm{W4}}, \quad (9)$$

where the SFR of each band is calculated using the model-based luminosity-to-SFR calibrations in Calzetti (2013). We adopt a fixed $D_{\rm L}$ of 21 Mpc for the Eridanus, NGC 1407 and NGC 1332 groups, and $D_{\rm L}$ for the background galaxies (see Table 3). The FUV/NUV and W4 luminosities indicate the dust unattenuated and attenuated part of the SFR, respectively. The FUV luminosities are preferred over the NUV in the estimates of SFR to minimize contamination from old stars, but when the FUV images are unavailable we use the

[8] *GALEX* images are retrieved from the Mikulski Archive Space Telescopes (MAST).

Table 5. Star formation rates.

ID	Designation	SFR_{FUV}	σ_{FUV}	SFR_{NUV}	σ_{NUV}	SFR_{W4}	σ_{W4}	SFR_{total}	σ_{total}	log SFR
		($M_\odot$ yr^{-1})	($M_\odot$ yr^{-1})	($M_\odot$ yr^{-1})	($M_\odot$ yr^{-1})	($M_\odot$ yr^{-1})	($M_\odot$ yr^{-1})	($M_\odot$ yr^{-1})	($M_\odot$ yr^{-1})	($M_\odot$ yr^{-1})
(1)	(2)	(3)	(4)	(5)	(6)	(7)	(8)	(9)	(10)	(11)
					Eridanus group					
1	WALLABY J032831−222957	0.012	0.241	0.002	0.081	...	...	0.012	0.241	−1.93
2	WALLABY J032900−220851	...	...	...	...	0.006	0.085	>0.006	0.085	>−2.22
3	WALLABY J032937−232103	0.015	0.101	0.004	0.075	...	...	0.015	0.101	−1.82
4	WALLABY J032941−221642	...	...	...	...	0.050	0.070	>0.050	0.070	>−1.30
5	WALLABY J033019−210832	...	...	...	...	0.007	0.098	>0.007	0.098	>−2.15
6	WALLABY J033047−210333	...	...	...	...	0.046	0.070	>0.046	0.070	>−1.34
7	WALLABY J033228−232245	0.012	0.276	0.002	0.075	...	...	0.012	0.276	−1.91
8	WALLABY J033257−210513	...	...	...	...	0.008	0.082	>0.008	0.082	>−2.10
9	WALLABY J033302−240756	0.034	0.090	0.006	0.067	...	...	0.034	0.090	−1.47
10	WALLABY J033326−234246	0.057	0.077	0.014	0.067	0.127	0.069	0.184	0.017	−0.74

Note. This table is available in its entirety as Supporting Information with the electronic version of the paper. A portion is shown here for guidance regarding its form and content. Columns (1)–(2): identification and designation. Columns (3)–(4): star formation rate and its error in the *GALEX* FUV. Columns (5)–(6): star formation rate and its error in the *GALEX* NUV. Columns (7)–(8): star formation rate and its error in the *NEOWISE* W4 band. Columns (9)–(10): total star formation rate and its error. Column (11): total star formation rate in the logarithmic scale.

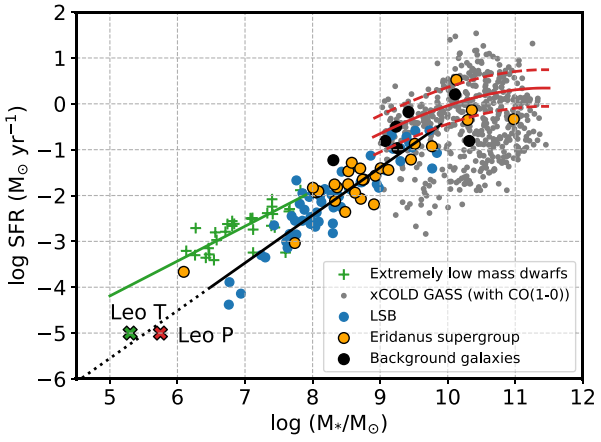

Figure 13. Star-forming main-sequence (SFMS) relation in logarithmic scale (log SFR versus log $M_*/M_\odot$). Eridanus supergroup and background galaxies in this study are represented by orange and black dots, respectively. xCOLD GASS (grey dots), LSB galaxies sample (blue dots), extremely low-mass dwarfs (green pluses), Leo T (green cross), and Leo P (red cross) are also plotted for comparison. The solid black and dashed lines represent the fit and extended relation from MG17. The solid and dashed red lines represent the fit and ±0.4 dex scatter boundaries from S17. The green solid line represents the fit from MQ21.

NUV luminosities instead. We note that all galaxies in our sample have FUV detections if they have FUV observations. For galaxies that are not detected in the W4 band (mostly low-mass galaxies), the dust attenuated part of the SFR is set to zero. If there is no FUV/NUV detection, the SFR is considered to be the lower limit. Table 5 summarises the star formation rates derived from various wavebands.

We investigate if our galaxies lie on the SFMS. The SFMS is a relation on the SFR–M_* plane. Galaxies that lie on this SFMS relation are actively forming stars, are quenched if they lie below, and are starbursting if they lie above. In Fig. 13, we show the fitted SFR–M_* relations derived from a sample of star-forming galaxies in extended CO Legacy Database for GASS (xCOLD GASS; Saintonge et al. 2017, hereafter S17) (red line), LSB galaxies (McGaugh, Schombert & Lelli 2017, hereafter MG17) (black line), and extremely low-mass dwarfs (MQ21) (green line). The xCOLD GASS data with CO(1–0) (grey dots) represent the SFMS relation derived for high-mass galaxies. The LSB galaxies data (blue dots) are at the low-mass end. The study of MG17 shows a steep slope for the SFMS using the low-mass samples but a flatter slope with the high-mass samples, which is similar to the relation derived with the xCOLD GASS samples. A shallower SFMS relation slope for a similar stellar mass range is seen in MQ21's study as compared to the MG17's study. This shallower SFMS relation is consistent with the SFMS relation derived from spiral galaxies. However, with a lower birth rate parameter, MQ21 find that a subset of the SHIELD sample galaxies would fall on to the steeper SMFS of MG17. This suggests that these subset of galaxies possess lower recent star formation that is similar to the star formation properties of LSB galaxies.

We also overplot Leo T (green cross), Leo P (red cross), our galaxies in the Eridanus supergroup (orange dots), and background galaxies (black dots) on to the SFR–M_* plane for comparison. Our lower mass ($<10^9$ $M_\odot$) Eridanus sample lies on the SFMS of MG17's study. Among the more massive galaxies ($>10^9$ $M_\odot$), three of them (ESO 482−G035, NGC 1422, and ESO 548−G021) lie below the S17 SFMS relation but on MG17's. The first two are H I deficient within the Eridanus group. ESO 548−G021 is H I normal within the NGC 1332 group. It is unclear if these galaxies are quenching due to them being located in the overlapping region of these two SFMS relations. The background galaxies are in general following the SFMS relation of S17 with one (LEDA 798516) slightly above MG17's but it is still within the scatter. LEDA 798516 is possibly interacting with surrounding galaxies and this could result in bursting of star formation. Leo T and Leo P fall on to the extended relation of MG17's, while the lowest stellar mass dwarf in our sample lies above it but closer to MQ21's.

8 ENVIRONMENT OF THE ERIDANUS SUPERGROUP

The cosmic web is referred as a network of filaments with clustered galaxies and gases stretched across the Universe and separated by voids (Pomarède et al. 2017). It is seen in simulations and maps derived from galaxy redshift surveys. The so-called the cosmic flow models are represented by the observed distribution of galaxies, peculiar velocities, and the underlying density field (see TCS16; Pomarède et al. 2017, for detail on Cosmic V-Web). In Fig. 14, we show

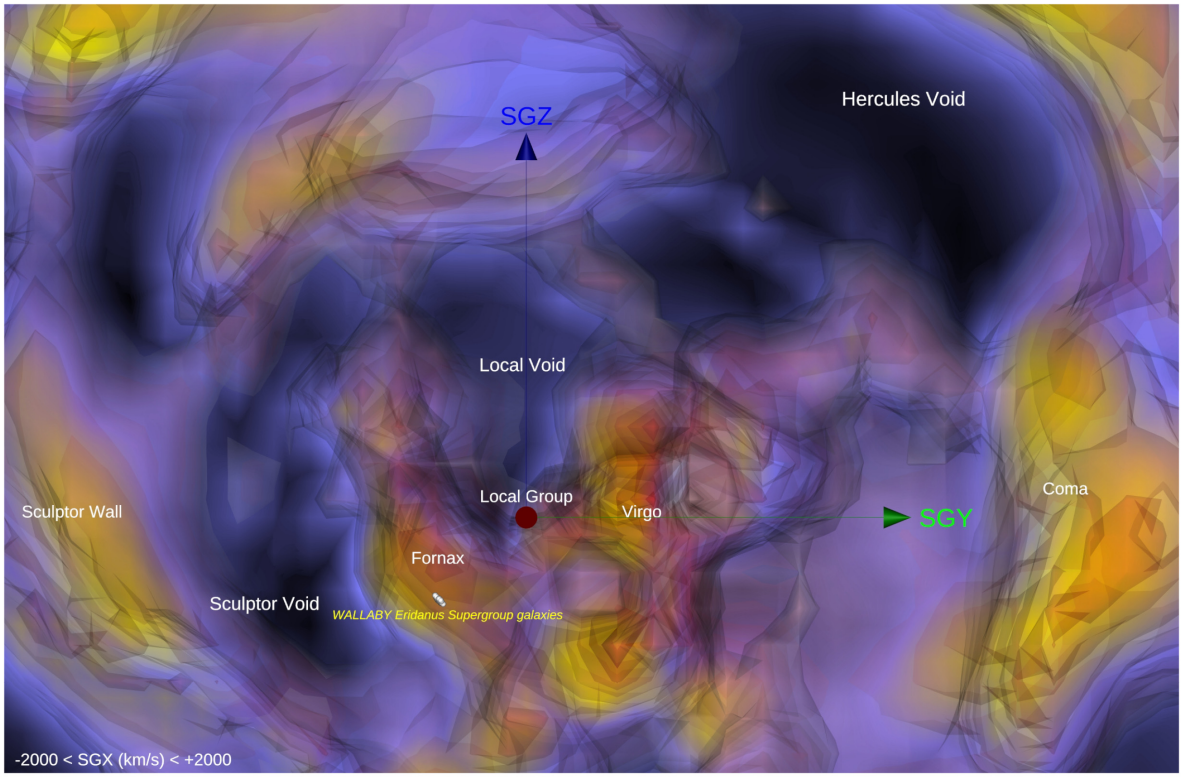

Figure 14. A slice of three-dimensional model contains planes within the SGX $= -2000$ km s^{-1} and $+2000$ km s^{-1} is shown face-on from the positive SGX direction. The positions of the Eridanus supergroup galaxies are plotted against a map of the density contrast δ reconstructed from the Cosmicflows-3 catalogue of peculiar velocities (Graziani et al. 2019). This map is obtained with the ray-casting volume rendering technique, resulting in a smooth representation of the δ field ranging from most underdense (deep blue colour) to most overdense (yellow), combined with a series of semitransparent isosurface polygons resulting in a sharp materialization of the surfaces ranging from $\delta = 0$ (grey surface) to highly overdense ($\delta = 2.8$ in red). The grey surface delineates the frontier between underdense and overdense patches of the local Universe. Scale and orientation are provided by the 5000 km s^{-1} long arrows emanating from our position and associated with the cardinal axes of the supergalactic coordinate system. An interactive three-dimensional model is available at https://sketchfab.com/3d-models/wallaby-eridanus-supergroup-versus-cf3-density-2d92e8a9f4b74f4293d9fabb9a6e73b3.

a three-dimensional slice of the Universe centred at supergalactic position SGX $= 0$ and the environment that the Eridanus supergroup resides in. The model is computed using the overdensity field, Δ, by the means of four isosurface levels, namely 0.5, 1.0, 1.5, and 2.0. We find that all 43 galaxies are located near the knot of Fornax. If we adopt a fixed $D_{\rm L}$ of 21 Mpc for all galaxies, we also find that all of them fall in the same $\Delta = 1.428$ grid. The eigenvalues λ_1, λ_2, and λ_3 of the shear tensor are 0.621, 0.090, and 0.030, respectively. The positive eigenvalues suggest that they are residing in a knot cell of the V-Web. However, the two lower eigenvalues (λ_2, λ_3) indicate that some are edging toward the Sculptor Void. Overall, the model suggests that Eridanus supergroup is currently merging/falling on to the Fornax V-Web knot. In future work, We will re-examine these findings with the derived individual distances from the Tully–Fisher relation paper.

9 SUMMARY AND CONCLUSIONS

We present the first WALLABY pre-pilot results from (almost) all the ASKAP antennas. These observations mimic the observation strategy for the WALLABY pilot survey. We assess the data quality by using a set of statistical metrics. We also perform source finding using SOFIA and obtain a catalogue of 55 H I sources within ∼37 MHz, including two H I clouds without stellar counterparts. In conjunction with deep optical images from the DR8 DESI Legacy Imaging Survey, we recover new gas-rich LSB galaxies and dwarfs. We compare the integrated fluxes of WALLABY with the HIPASS and Parkes basketweave Eridanus survey. This reveals a 20 per cent deficit of integrated flux for the pre-pilot observations, which appears to arise from an accumulation of flux density scale errors, missing extended flux, low S/N ratio, and the use of inaccurate primary beam models for the edge beams. All of these are better addressed in the WALLABY pilot survey data. In the meantime, a uniform 20 per cent correction is applied to the Eridanus fluxes for statistical purposes. Based on the galaxy group catalogues of G93, T15, and B06, we redefine membership of the Eridanus supergroup for our analysis. The mean recession velocity of the Eridanus group is ∼1500 km s^{-1}.

We also perform *g*- and *r*-band photometry measurements using PROFOUND and derive the corresponding stellar mass based on the *M*/*L*–colour relation in B03. By comparing with a more recently derived *M*/*L*–colour relation of Z09, we find that the stellar masses are generally consistent except for one low-mass galaxy. We also calculate the H I masses and the H I deficiency parameter. The H I masses of Eridanus group and background galaxies range from $10^{7.5-9.8}$ and $10^{9-10.1}$ M$_\odot$, respectively. There are 20 galaxies in the Eridanus group considered to be H I deficient (DEF$_{\rm H\,I} > 0.3$ dex) and most of them are near other H I detected sources. All galaxies show signs of disturbance in their H I morphology. Both tidal interaction and ram-pressure stripping mechanisms contribute gas loss in the Eridanus group (Murugeshan et al. 2021). There is no correlation

between the H I deficiency parameter and the projected distance from the Eridanus group centre.

Two massive previously known H I clouds have been detected (see Wong et al. 2021). Smaller H I clouds are also detected as part of a single source detection. The most prominent tidal debris field is seen in NGC 1359 (an interacting pair) and NGC 1385. This debris has no optical counterpart. Some galaxies also show evidence of extraplanar gas extending out of the disc.

Comparing the gas fraction scaling relation with xGASS and the study of Maddox et al. (2015), we find that the gas fraction of background galaxies follows the general trend of decreasing $M_{\rm H\,I}/M_*$ with increasing M_*. However, the gas fraction of galaxies in the Eridanus supergroup is lower for a given M_*. To further investigate if the lower gas fraction trend is real in the Eridanus supergroup, we run a H I detection limit test. We find that a lower gas fraction trend remains for the galaxies in the Eridanus supergroup. We also compare the galaxies in the Eridanus supergroup with the gas fraction of dwarfs in the Local Group. The trend of $M_{\rm H\,I}/M_*$ versus M_* among the Local Group dwarf population is not clear but an indication of various H I scaling relations is needed for different environment density.

To investigate if galaxies in our study are actively forming stars, we compare them with the SFMS determined by S17, MG17, and MQ21. Overall, our galaxies in the Eridanus supergroup and background galaxies are actively forming stars. We rule out the possibility of a gas accreting event given that they generally follow the gas fraction scaling relation in the high-mass regime.

ACKNOWLEDGEMENTS

This research was supported by the ARC Centre of Excellence for All Sky Astrophysics in 3 Dimensions (ASTRO 3D), through project number CE170100013. PK is partially supported by the BMBF project 05A17PC2 for D-MeerKAT. LV-M acknowledges financial support from the grants AYA2015-65973-C3-1-R and RTI2018-096228-B-C31 (MINECO/FEDER, UE), as well as from the State Agency for Research of the Spanish MCIU through the 'Center of Excellence Severo Ochoa' award to the Instituto de Astrofisica de Andalucia (SEV-2017-0709). The Australian SKA Pathfinder is part of the Australia Telescope National Facility that is funded by the Australian Government with support from the National Collaborative Research Infrastructure Strategy and Industry Endowment Fund. ASKAP uses the resources of the Pawsey Supercomputing Centre with funding provided by the Australian Government under the National Computational Merit Allocation Scheme (project JA3). We acknowledge the Wajarri Yamatji as the traditional owners of the Murchison Radio Observatory (MRO) site and thank the operational staff on-site. This research has made use of images of the Legacy Surveys. The Legacy Surveys consist of three individual and complementary projects: the Dark Energy Camera Legacy Survey (DECaLS; Proposal ID #2014B-0404; PIs: David Schlegel and Arjun Dey), the Beijing–Arizona Sky Survey (BASS; NOAO Prop. ID #2015A-0801; PIs: Zhou Xu and Xiaohui Fan), and the Mayall z-band Legacy Survey (MzLS; Prop. ID #2016A-0453; PI: Arjun Dey). DECaLS, BASS, and MzLS together include data obtained, respectively, at the Blanco telescope, Cerro Tololo Inter-American Observatory, NSF's NOIRLab; the Bok telescope, Steward Observatory, University of Arizona; and the Mayall telescope, Kitt Peak National Observatory, NOIRLab. The Legacy Surveys project is honoured to be permitted to conduct astronomical research on Iolkam Du'ag (Kitt Peak), a mountain with particular significance to the Tohono O'odham Nation. B-QF thanks A. Robotham and L. Davies for assisting the use ProFound and VISTA-view cutout service.

DATA AVAILABILITY

The data underlying this paper are available in the paper and in its online supplementary material. The processed ASKAP data can be retrieved via CSIRO ASKAP Science Data Archive (CASDA) with a given scheduling block identification number. The DOI for the Eridanus data is https://doi.org/10.25919/kqrt-pv24. The data products from SOFIA is currently available within the WALLABY team and will be release to the public at a later date.

REFERENCES

Abramson A., Kenney J. D. P., Crowl H. H., Chung A., van Gorkom J. H., Vollmer B., Schiminovich D., 2011, AJ, 141, 164
Adams E. A. K., Oosterloo T. A., 2018, A&A, 612, A26
Baker R. H., 1933, Ann. Harvard College Obser., 88, 77
Barnes D. G. et al., 2001, MNRAS, 322, 486
Begum A., Chengalur J. N., Karachentsev I. D., Sharina M. E., Kaisin S. S., 2008, MNRAS, 386, 1667
Bekki K., Couch W. J., Ryan-Weber E. V., Webster R. L., 2004, in Duc P.-A., Braine J., Brinks E., eds, Proc. IAU Symp. 217, Recycling Intergalactic and Interstellar Matter. Astron. Soc. Pac., San Francisco, p. 418
Bell E. F., McIntosh D. H., Katz N., Weinberg M. D., 2003, ApJS, 149, 289 (B03)
Boselli A., Cortese L., Boquien M., Boissier S., Catinella B., Lagos C., Saintonge A., 2014, A&A, 564, A66
Brough S., Forbes D. A., Kilborn V. A., Couch W., Colless M., 2006, MNRAS, 369, 1351 (B06)
Calzetti D., 2013, in Falcón-Barroso J., Knapen J. H., eds, Secular Evolution of Galaxies. Cambridge Univ. Press, Cambridge, p. 419
Cardelli J. A., Clayton G. C., Mathis J. S., 1989, ApJ, 345, 245
Catinella B. et al., 2018, MNRAS, 476, 875
Chabrier G., 2003, PASP, 115, 763
Chung A., van Gorkom J. H., Kenney J. D. P., Crowl H., Vollmer B., 2009, AJ, 138, 1741
Condon J. J., Cotton W. D., Greisen E. W., Yin Q. F., Perley R. A., Taylor G. B., Broderick J. J., 1998, AJ, 115, 1693
Cornwell T. J., 2008, IEEE J. Selected Topics Signal Processing, 2, 793
Cortese L. et al., 2019, MNRAS, 485, 2656
Cortese L., Catinella B., Smith R., 2021, PASA, 38, 35
da Costa L. N. et al., 1988, ApJ, 327, 544
Dénes H., Kilborn V. A., Koribalski B. S., 2014, MNRAS, 444, 667 (D14)
de Vaucouleurs G., 1975, in Sandage A., Sandage M., Kristian J., eds, Galaxies and the Universe. Univ. Chicago Press, Chicago, IL, p. 557
Dey A. et al., 2019, AJ, 157, 168
Dressler A., 1980, ApJ, 236, 351
Elagali A. et al., 2019, MNRAS, 487, 2797
Escudero C. G., Faifer F. R., Smith Castelli A. V., Forte J. C., Sesto L. A., González N. M., Scalia M. C., 2018, MNRAS, 474, 4302
Fitzpatrick E. L., 1999, PASP, 111, 63
Fixsen D. J., Cheng E. S., Gales J. M., Mather J. C., Shafer R. A., Wright E. L., 1996, ApJ, 473, 576
For B. Q., Staveley-Smith L., Matthews D., McClure-Griffiths N. M., 2014, ApJ, 792, 43
For B. Q. et al., 2019, MNRAS, 489, 5723
Forbes D. A., Sánchez-Blázquez P., Phan A. T. T., Brodie J. P., Strader J., Spitler L., 2006, MNRAS, 366, 1230
Garcia A. M., 1993, A&AS, 100, 47 (G93)
Garcia A. M., Paturel G., Bottinelli L., Gouguenheim L., 1993, A&AS, 98, 7 (G93)
Giovanelli R. et al., 2005, AJ, 130, 2598
Gómez P. L. et al., 2003, ApJ, 584, 210

Graziani R., Courtois H. M., Lavaux G., Hoffman Y., Tully R. B., Copin Y., Pomarède D., 2019, MNRAS, 488, 5438
Grcevich J., Putman M. E., 2009, ApJ, 696, 385
Haynes M. P., Giovanelli R., 1984, AJ, 89, 758
Hibbard J. E., van Gorkom J. H., 1996, AJ, 111, 655
Hickson P., 1997, ARA&A, 35, 357
Hotan A. W. et al., 2021, Publ. Astron. Soc. Aust., 38, e009
Hoyle B., Masters K. L., Nichol R. C., Jimenez R., Bamford S. P., 2012, MNRAS, 423, 3478
Huang S., Haynes M. P., Giovanelli R., Brinchmann J., Stierwalt S., Neff S. G., 2012, AJ, 143, 133
Johnston S. et al., 2007, Publ. Astron. Soc. Aust., 24, 174
Jones D. H. et al., 2004, MNRAS, 355, 747
Jones M. G. et al., 2018, A&A, 609, A17
Katz N., Keres D., Dave R., Weinberg D. H., 2003, in Rosenberg J. L., Putman M. E., eds, ASSL Conf. Proc. Vol. 281, The IGM/Galaxy Connection: The Distribution of Baryons at z=0. Kluwer, Dordrecht, p. 185
Kenney J. D. P., van Gorkom J. H., Vollmer B., 2004, AJ, 127, 3361
Kereš D., Katz N., Weinberg D. H., Davé R., 2005, MNRAS, 363, 2
Kilborn V. A., Forbes D. A., Koribalski B. S., Brough S., Kern K., 2006, MNRAS, 371, 739
Kilborn V. A., Forbes D. A., Barnes D. G., Koribalski B. S., Brough S., Kern K., 2009, MNRAS, 400, 1962
Kleiner D. et al., 2019, MNRAS, 488, 5352
Koribalski B. S. et al., 2018, MNRAS, 478, 1611
Koribalski B. S. et al., 2020, Ap&SS, 365, 118
Kundu A., Whitmore B. C., 2001, AJ, 122, 1251
Lee-Waddell K. et al., 2019, MNRAS, 487, 5248
Li J., Obreschkow D., Lagos C., Cortese L., Welker C., Džudžar R., 2020, MNRAS, 493, 5024
McConnell D. et al., 2016, Publ. Astron. Soc. Aust., 33, e042
McConnell D. et al., 2020, Publ. Astron. Soc. Aust., 37, e048
McGaugh S. S., Schombert J. M., Lelli F., 2017, ApJ, 851, 22 (MG17)
McQuinn K. B. W. et al., 2015, ApJ, 812, 158
McQuinn K. B. W. et al., 2021, preprint (arXiv:2105.05100) (MQ21)
Madau P., Dickinson M., 2014, ARA&A, 52, 415
Maddox N., Hess K. M., Obreschkow D., Jarvis M. J., Blyth S. L., 2015, MNRAS, 447, 1610
Mahajan S., 2013, MNRAS, 431, L117
Marinoni C., Monaco P., Giuricin G., Costantini B., 1998, ApJ, 505, 484
Martin D. C. et al., 2005, ApJ, 619, L1
Masci F. J., Fowler J. W., 2009, in Bohlender D. A., Durand D., Dowler P., eds, ASP Conf. Ser. Vol. 411, Astronomical Data Analysis Software and Systems XVIII. Astron. Soc. Pac., San Francisco, p. 67
Materne J., 1978, A&A, 63, 401
Meyer M. J. et al., 2004, MNRAS, 350, 1195
Meyer M., Robotham A., Obreschkow D., Westmeier T., Duffy A. R., Staveley-Smith L., 2017, Publ. Astron. Soc. Aust., 34, e052
Morshidi-Esslinger Z., Davies J. I., Smith R. M., 1999, MNRAS, 304, 311
Murugeshan C. et al., 2021, MNRAS, preprint (arXiv:2108.04414)
Obreschkow D., Glazebrook K., Kilborn V., Lutz K., 2016, ApJ, 824, L26
Omar A., Dwarakanath K. S., 2005a, J. Astrophys. Astron., 26, 1
Omar A., Dwarakanath K. S., 2005b, J. Astrophys. Astron., 26, 71
Paturel G., Bottinelli L., Fouque P., Gouguenheim L., 1988, in Murtagh F., Heck A., eds, ESO Conf. Workshop Proc. No. 28, Astronomy from Large Databases: Scientific Objectives and Methodological Approaches. European Southern Observatory, München, Germany, p. 435
Pisano D. J., 2014, AJ, 147, 48
Pomarède D., Hoffman Y., Courtois H. M., Tully R. B., 2017, ApJ, 845, 55
Postman M. et al., 2005, ApJ, 623, 721
Putman M. E., Zheng Y., Price-Whelan A. M., Grcevich J., Johnson A. C., Tollerud E., Peek J. E. G., 2021, ApJ, 913, 53
Reynolds T. N. et al., 2019, MNRAS, 482, 3591
Richtler T., 2003, in Alloin D., Gieren W., eds, Lecture Notes in Physics Vol. 635, Stellar Candles for the Extragalactic Distance Scale. Springer-Verlag, Berlin, p. 281
Robotham A. S. G., Davies L. J. M., Driver S. P., Koushan S., Taranu D. S., Casura S., Liske J., 2018, MNRAS, 476, 3137
Ryan-Weber E., Webster R., Bekki K., 2003, in Rosenberg J. L., Putman M. E., eds, ASSL Conf. Proc. Vol. 281, The IGM/Galaxy Connection: The Distribution of Baryons at z=0. Kluwer, Dordrecht, p. 223
Ryan-Weber E. V., Begum A., Oosterloo T., Pal S., Irwin M. J., Belokurov V., Evans N. W., Zucker D. B., 2008, MNRAS, 384, 535
Saintonge A. et al., 2017, ApJS, 233, 22 (S17)
Salpeter E. E., 1955, ApJ, 121, 161
Schlafly E. F., Finkbeiner D. P., 2011, ApJ, 737, 103
Schlegel D. J., Finkbeiner D. P., Davis M., 1998, ApJ, 500, 525
Serra P., Jurek R., Flöer L., 2012, Publ. Astron. Soc. Aust., 29, 296
Serra P. et al., 2015, MNRAS, 448, 1922
Simard L. et al., 2009, A&A, 508, 1141
Solanes J. M., Giovanelli R., Haynes M. P., 1996, ApJ, 461, 609
Sorgho A. et al., 2019, MNRAS, 482, 1248
Spergel D. N. et al., 2007, ApJS, 170, 377
Springob C. M., Haynes M. P., Giovanelli R., Kent B. R., 2005, ApJS, 160, 149
Tully R. B., 1980, ApJ, 237, 390
Tully R. B., 2015, AJ, 149, 171 (T15)
Tully R. B., Courtois H. M., Sorce J. G., 2016, AJ, 152, 50 (TCS16)
Verdes-Montenegro L., Yun M. S., Williams B. A., Huchtmeier W. K., Del Olmo A., Perea J., 2001, A&A, 377, 812
Walter F., Brinks E., de Blok W. J. G., Bigiel F., Kennicutt R. C., Jr, Thornley M. D., Leroy A., 2008, AJ, 136, 2563
Wang J. et al., 2017, MNRAS, 472, 3029 (W17)
Waugh M., 2005, PhD thesis, Univ. Melbourne, Melbourne
Westmeier T., Staveley-Smith L., Calabretta M., Jurek R., Koribalski B. S., Meyer M., Popping A., Wong O. I., 2015, MNRAS, 453, 338
Westmeier T. et al., 2017, MNRAS, 472, 4832
Westmeier T. et al., 2021, MNRAS, 506, 3962
Whiting M. T., 2020, in Ballester P., Ibsen J., Solar M., Shortridge K., eds, ASP Conf. Ser. Vol. 522, Astronomical Data Analysis Software and Systems XXVII. Astron. Soc. Pac., San Francisco, p. 469
Wieringa M., Raja W., Ord S., 2020, in Pizzo R., Deul E. R., Mol J. D., de Plaa J., Verkouter H., eds, ASP Conf. Ser. Vol. 527, Astronomical Data Analysis Software and Systems XXIX. Astron. Soc. Pac., San Francisco, p. 591
Willmer C. N. A., 2018, ApJS, 236, 47
Willmer C. N. A., Focardi P., da Costa L. N., Pellegrini P. S., 1989, AJ, 98, 1531
Wolfinger K., Kilborn V. A., Ryan-Weber E. V., Koribalski B. S., 2016, Publ. Astron. Soc. Aust., 33, e038
Wong O. I. et al., 2021, MNRAS, preprint (arXiv:2108.04412)
Zabludoff A. I., Mulchaey J. S., 1998, ApJ, 496, 39
Zibetti S., Charlot S., Rix H.-W., 2009, MNRAS, 400, 1181 (Z09)

SUPPORTING INFORMATION

Supplementary data are available at *MNRAS* online.

Table 3. Source catalogue and derived parameters.
Table 4. Photometry, morphology, and derived parameters.
Table 5. Star formation rates.
Figure 5. Examples of WALLABY H I sources.

Please note: Oxford University Press is not responsible for the content or functionality of any supporting materials supplied by the authors. Any queries (other than missing material) should be directed to the corresponding author for the article.

APPENDIX A: H I AND OPTICAL MORPHOLOGIES

In this section, we examine the H I and optical morphologies of galaxies. We refer the reader to Figs 4 and 5 for H I optical morphologies and ID number of galaxies. All of the galaxies in the Eridanus supergroup show signs of disturbance in H I morphology.

The H I detection of NGC 1347 (#4) includes its interacting galaxy, PGC 816443. An H I extension is visible at $N_{\rm H\,I} \sim 5 \times 10^{20}$ cm^{-2}. LEDA 832131 (#5) does not have a morphological classification in NED. We identify it as an irregular dwarf with multiple star-forming regions visible in the optical image. It is located to the south-west of both ESO 548−G029 (#6) and ESO 548−G034 (#8), which are also distorted in H I morphology. This indicates that the three are likely interacting with each other. ESO 548−G036 (#11) is located south-west of IC 1953 (#12). There is strong evidence that these two galaxies are interacting with an H I extension seen in IC 1953 towards ESO 548−G036. An H I cloud is also detected north of ESO 548−G036. NGC 1385 (#20) is a face-on spiral galaxy that is located 0.°6 south of WALLABY J033723−235753. Its H I morphology is much distorted and there is a southern tidal debris field. There is no optical counterpart for the H I debris. ESO 482−G035 (#29) is a face-on SBab galaxy with a distorted and elongated H I morphology, which is in contrast to the non-fully developed H I disc as shown in Omar & Dwarakanath (2005b). There is also a known LSB dwarf, F482−018 (Morshidi-Esslinger, Davies & Smith 1999), south of ESO 482−G035, which does not have an H I detection. Given the elongation of the H I, this dwarf could potentially be a satellite of ESO 482−G035. GALEXASC J033408.06−232130.1 (#13; $\mathrm{DEF_{H\,I}} = -0.83$) is a LSB dwarf and we find a H I cloud is seen on the eastern side of this galaxy. ESO 482−G005 (#9; $\mathrm{DEF_{H\,I}} = -0.29$) is an edge-on galaxy. Both galaxies show signatures of disturbance.

NGC 1422 (#30) shows a truncated H I disc that is smaller than the stellar disc. LEDA 135119 (#33) is classified as a spiral galaxy in NED but no distinctive spiral arms are seen in our optical image. Its H I morphology is asymmetric and an H I cloud north of the galaxy is detected. It is located at the edge of the observed field, and hence, we cannot rule out the possibility that the galaxy is interacting with another nearby galaxy. Both NGC 1398 (#21) and NGC 1415 (#27) are large bright galaxies with *B*-band optical isophotal diameter measured at 25 mag arcsec^{-2} of 425 and 208 arcsec, respectively. The H I traces various star-forming sites and is extended beyond the optical disc. NGC 1398 (SBab galaxy) also has a ring-like H I that resembles a similar feature as seen in NGC 1533 (Ryan-Weber, Webster & Bekki 2003). Modelling of NGC 1533 suggests that the ring-like H I is formed as a result of an unequal-mass merging event between gas-rich LSB galaxies and host SB galaxy's disc (Bekki et al. 2004). NGC 1398 is located at the edge of the observed field and furthest from the Eridanus group centre. NGC 1438 (#35) is a SB0/a galaxy that has a peculiar H I morphology. There are two tidal tails south of the galaxy and no optical counterpart has been identified along the tails.

Other interesting H I morphologies within the Eridanus group include ESO 482−G013 (#18) and ESO 482−G027 (#24). There are H I extensions seen above and below the H I disc of ESO 482−G013 (#18). Some edge-on galaxies also show evidence of extraplanar gas with plumes of gas extended out of the disc (e.g. IC 1952, ESO 482−G013, and ESO 482−G011). The latter is an irregular galaxy and its H I morphology resembles a head–tail structure with the tail pointing away from the Eridanus group centre. It is also located 0.°53 and 1.°46 angular distance from the two massive H I clouds, WALLABY J033723−235753 (#19) and WALLABY J033911−222322 (#22). We refer the reader to Wong et al. (2021) for the discussion of the origin of these two H I clouds.

Among the three detections in the NGC 1407 group, a large and spectacular H I tidal debris field is seen around the NGC 1359, an interacting galaxy pair (#41). Both ESO 548−G065 (#43) and NGC 1390 (#42) show disruption of the H I outer disc. Within the NGC 1332 group, NGC 1325 (#38) is a SAbc galaxy that forms a pair along with NGC 1325A. There is no H I detection of NGC 1325A in our study but there is in W15. Evidence of interaction is seen with gas extending from the north corner of LSB galaxy, ESO 548-G011 (#39), towards NGC 1325.

The H I morphology of all background galaxies also shows signs of disturbance. ESO 549−G023 (#50) is a SBa galaxy and is also classified as an emission line galaxy. It has an extended H I 'tail' toward the south-east and some small H I debris to the north-east of the galaxy. LEDA 798516 (#48) is a LSB galaxy and is possibly interacting with a few galaxies south of it, including LEDA 798377 (unresolved). Another H I detection is also seen at the north-east side of LEDA 798516. The location coincides with an edge-on galaxy (GALEXASC J033838.83−233810.9), which is not identified as a separate source by SOFIA.

This paper has been typeset from a TEX/LATEX file prepared by the author.